Author/s:
Manovski, P;Abu Rowin, W;Ng, H;Gulotta, P;Giacobello, M;de Silva, C;Hutchins, N;Marusic, I

Title:
The spectral response of time-resolved PIV in a turbulent boundary layer

Date:
2025

Citation:
Manovski, P., Abu Rowin, W., Ng, H., Gulotta, P., Giacobello, M., de Silva, C., Hutchins, N. & Marusic, I. (2025). The spectral response of time-resolved PIV in a turbulent boundary layer. Experiments in Fluids, 66 (7), https://doi.org/10.1007/s00348-025-04059-0.

Persistent Link:
https://hdl.handle.net/11343/362104

Experiments in Fluids (2025) 66:134
https://doi.org/10.1007/s00348-025-04059-0

RESEARCH ARTICLE

The spectral response of time-resolved PIV in a turbulent boundary layer

Peter Manovski[1,2] · Wagih Abu Rowin[2] · Henry Ng[1,3] · Paul Gulotta[4] · Matteo Giacobello[1] · Charitha de Silva[5] · Nicholas Hutchins[2] · Ivan Marusic[2]

Received: 23 December 2024 / Revised: 4 April 2025 / Accepted: 17 May 2025 / Published online: 13 June 2025

Abstract

This study presents the application of time-resolved particle image velocimetry (TR-PIV) to measure the mean and fluctuating velocity components in a turbulent boundary layer (TBL) over an axisymmetric body of revolution. A narrow wall-normal strip of the flow was captured using a synchronised high-speed laser and camera at a recording frequency of up to 80 kHz. The resulting streamwise and wall-normal velocity TR-PIV data were validated against hot-wire anemometry measurements and direct numerical simulations (DNS) of a flat plate under matched flow conditions. The mean flow results showed good agreement between all methods, while the expected attenuation due to the spatial averaging was found in the TR-PIV turbulence statistics closer to the wall. A key outcome of this study is the establishment of an effective laser sheet thickness for the TR-PIV using DNS as a reference. This study fills a gap in understanding the spectral response and limitations of TR-PIV in such complex flows, particularly how spatial resolution and noise influence the accuracy of turbulence measurements. The TR-PIV streamwise velocity energy spectra were compared with DNS data that were spatially filtered to match the resolution of the TR-PIV and hot-wire. A transfer function was derived to determine cut-off wavelengths as a function of wall-normal distance. The cut-off wavelengths enabled the quantification of the resolvable turbulence scales within the TBL, revealing that the spatial resolution is a limiting factor for TR-PIV. The methodology was applied to locations with zero and favourable pressure gradients, providing insights into how pressure gradients influence spectral content and the limitations of TR-PIV in capturing the full range of turbulence scales. The outlined methodology is applicable more broadly and can be used to enhance the accuracy of experimental techniques in future boundary layer investigations.

1 Introduction

The accurate measurement and analysis of turbulent boundary layers (TBLs) are critical for advancing our understanding of wall-bounded flows and improving experimental methodologies. Among the available techniques, time-resolved particle image velocimetry (TR-PIV) has emerged as a powerful tool for capturing the temporal and spatial dynamics of turbulence. A recent review by Beresh (2021) highlights TR-PIV's ability to provide detailed insights into turbulent flows, including spectral content, two-point and space-time correlations, modal analysis and integral timescales. However, its performance in wall-bounded flows, particularly in challenging conditions involving pressure gradients and small-scale turbulence, requires further evaluation to establish its limitations and potential.

This study employs TR-PIV to investigate the TBL at two locations along a geometry that provides a range of flow conditions, including near-zero pressure gradient (ZPG) and mild favourable pressure gradient (FPG). Measurements are conducted over an axisymmetric body of revolution, which serves as a practical test case to evaluate TR-PIV's capability to resolve turbulence across varying flow scales and pressure gradients.

✉ Peter Manovski
peter.manovski@defence.gov.au

[1] Defence Science and Technology Group, Melbourne 3207, Australia

[2] Department of Mechanical Engineering, University of Melbourne, Melbourne 3010, Australia

[3] School of Engineering, University of Liverpool, Liverpool L69 3GH, UK

[4] Air Force Institute of Technology, Wright-Patterson AFB, Ohio 45433, USA

[5] School of Mechanical and Manufacturing Engineering, University of New South Wales, Sydney 2052, Australia

The TR-PIV method used here takes inspiration from Willert (2015, 2018). In this method, a narrow strip of the flow field is illuminated by a high-speed laser and imaged by a high-speed camera to provide very high capture rates, allowing TR-PIV velocity measurements. The TR-PIV employed here pushes the current limits of camera and laser technology, with repetition rates up to 80 kHz and acquisition time sufficient to enable long data series (up to 800,000 samples) suitable for converged statistical quantities and the extraction of the full broadband spectral energy content.

Building upon studies outlined by Beresh (2021), we present a detailed investigation of the spectral energy content, incorporating comparisons with highly resolved hot-wire anemometry and direct numerical simulations (DNS) of a flat plate to clarify the impact of temporal and spatial resolution on resolvable flow scales, particularly as a function of wall height and pressure gradients. As noted by Beresh (2021), the term "time-resolved" is often loosely defined in fluid mechanics, with the fundamental criterion being that the temporal resolution must be sufficient to capture the relevant flow timescales, including the smallest, fastest eddies responsible for energy dissipation. Here, we rigorously assess the validity of time-resolved measurements in wall-bounded flows through spectral analysis against hot-wire and DNS benchmarks, ensuring that the majority of the energy content within the temporal bandwidth is accurately captured.

It is also important to consider the coupling between spatial and temporal resolutions for TR-PIV measurements. A high temporal resolution must be complemented by adequate spatial resolution to ensure coherent structures in the flow are accurately captured and not smeared out. As such, TR-PIV also has a temporal cut-off due to the finite PIV spatial resolution or interrogation window (*IW*) size (Willert 2015; Atkinson et al. 2015). A larger *IW* will average the velocities of particles over a more significant spatial extent. This smoothing can lead to underestimation of the velocity and changes in the turbulent fluctuations, effectively reducing the temporal resolution of the measurement. Understanding these aspects is crucial; however, the literature is limited. This is particularly important for flows containing varying pressure gradients, where the contribution of different flow scales changes for varying pressure gradients. Furthermore, the influence of particle lag (due to particle size and density) is also explored in spectral space, again as a function of wall distance.

Particle tracking velocimetry (PTV) can provide superior spatial resolution and only exhibits minimal spatial averaging (or attenuation of turbulence levels) compared with PIV (Kähler et al. 2012). The TR-PIV provides a highly temporally resolved dataset to enable the use of PTV from PIV using correlation (Stanislas et al. 2005; Theunissen et al. 2008). Thus, PTV will complement the TR-PIV data by providing highly resolved statistical quantities of the TBL, including mean velocity profiles and Reynolds stress distributions.

As performed by Foucaut et al. (2004), spectral analysis on PIV data was instrumental in characterising and modelling inherent noise. In a complementary study, Atkinson et al. (2013) explored filtering methods for PIV in TBL flows, using spectral analysis to match filtered results with spatially filtered DNS of equivalent resolution. Atkinson et al. (2015) applied these methods to TR-PIV of a TBL at a lower Reynolds number (*Re*) than our study in a water tunnel with hollow glass spheres as tracers. In contrast, this study uses TR-PIV in a large-scale wind tunnel with aerosol tracers on an axisymmetric model, pushing acquisition rates to camera limits and capturing longer sequences for broader spectral analysis. These conditions challenge particle imaging, potentially altering noise characteristics, while the large-scale facility limits spatial resolution. Atkinson et al. (2013, 2015) derived transfer functions between PIV and DNS spectra, linking TR-PIV and DNS spectral content across spatial scales. Our study extends this by deriving cut-off wavelengths as a function of wall-normal distance, quantifying spectral attenuation limits and assessing TR-PIV's ability to resolve fine-scale turbulence in the TBL. This methodology, applied at ZPG and FPG locations, evaluates pressure gradient effects on spectral characteristics and TR-PIV limitations. We further explore noise mitigation through select PIV processing and denoising filters, analysing their impact on turbulence and spectral response. This analysis directly addresses a question posed by Beresh (2021) on the resultant effects of PIV processing and filtering methods on the overall spectral response.

1.1 Background and context for the test geometry

The axisymmetric body of revolution geometry used in this study is based on a conventional diesel-electric submarine concept design by Joubert (2006) and is shown in Fig. 1. The geometry is commonly referred to as the baseline or bare hull variant, without casing and appendages. It is considered canonical due to its streamlined elliptical nose, cylindrical mid-body section, and streamlined tail designed to minimise flow separation. Accurate measurements of the TBL flow, turbulence levels, and spectral content are critical to understanding flow behaviour around such geometries. Further information on the geometry and references to the past studies can be found in the supplementary material (S1).

For axisymmetric TBLs, Piquet and Patel (1999) parameterised the effects of transverse curvature using two parameters. Firstly, the curvature parameter, which is the ratio of the boundary layer thickness (δ) to local radius of curvature (a). Secondly, the radius of curvature in wall units (a^+) also referred to as the radius Reynolds number (Re_{a^+}), where the

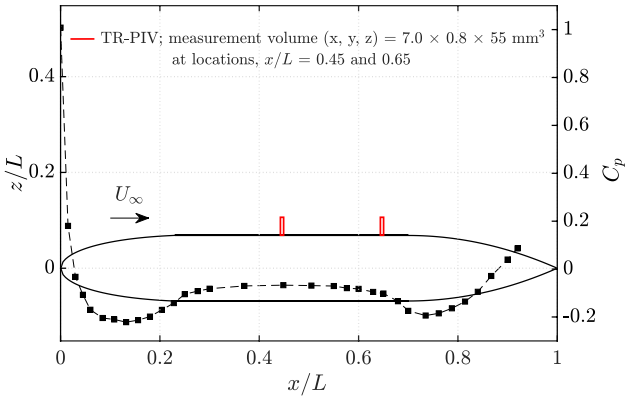

Fig. 1 A schematic of the axisymmetric body of revolution, showing the coefficient of pressure (C_p) axial distribution with black filled symbols (■), and the TR-PIV measurement area and locations (red rectangles). The flow is from left-to-right, as indicated with the freestream flow vector

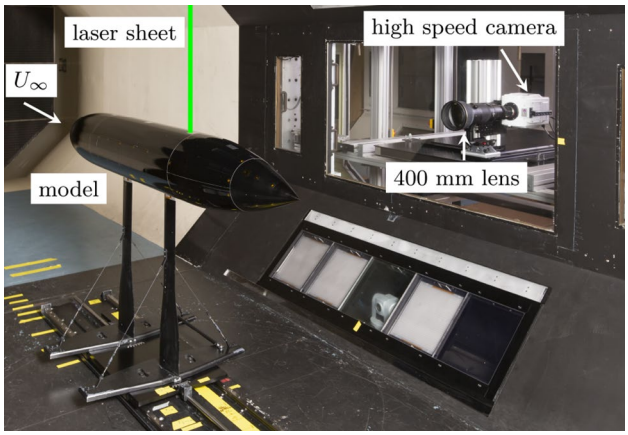

Fig. 2 Photograph of the axisymmetric body of revolution model and TR-PIV experimental setup, showing camera, lens, the laser sheet and the model, mounted with twin aerofoil-sectioned supports

superscript '+' indicates inner normalisation by friction velocity U_τ and kinematic viscosity, ν. For practical vehicle applications, the most relevant case identified by Piquet and Patel (1999) is when the curvature parameter is small or of order one ($a/\delta \ll \mathcal{O}(1)$) and a^+ is large ($\gtrsim 200$, where the layer is turbulent). This corresponds to relatively high Reynolds number (Re_τ) flow where the local body radius is large relative to the very thin boundary layer and curvature effects are minimal, such that TBL characteristics appear very similar to a planar or 2D TBL. For the current geometry, this was indeed found to be the case at axial location, $x/L = 0.45$ where a ZPG exists, and the curvature parameter is small ($a/\delta = 0.1$) (Manovski et al. 2020, 2022b).

The structure of the paper is as follows. Section 2 provides a detailed description of the test facility and model, followed by the experimental methodologies in Sect. 3. The theoretical analysis of TR-PIV cut-off frequencies is covered in Sect. 4. The results and their discussion are presented in Sect. 5, and some concluding remarks are made in Sect.6.

2 Test facility and model

All tests were conducted in a large-scale closed-circuit wind tunnel, at the Defence Science and Technology Group in Melbourne, with a test section that is an irregular octagon, 2.74 m wide, 2.13 m high, and 6.56 m long. The freestream streamwise turbulence intensity is less than 0.4%, and the individual transverse intensities are less than 0.7% (Erm 2003; Manovski et al. 2023).

The test model is shown in Fig. 2 and has a length (L) of 2000 mm and a diameter (D) of 273.66 mm. The model was mounted on a twin aerofoil sliding rail support as shown in Fig. 2. A detailed description of the model geometry can be found in Manovski et al. (2020). The model was tested at zero incidence with an oncoming airspeed of 28.8–30 m/s (dependent on the local temperature), while the Reynolds number based on the length of the model was $Re_L \approx LU_\infty/\nu \approx 3.95 \times 10^6$ and held nominally constant during the various tests. The test Re_L was chosen to match previous experimental tests (Manovski et al. 2020). Following the guidelines of Barlow et al. (1999), the total blockage results in no more than 1% change in the flow speed. As described in Manovski et al. (2020), a circumferential ring of trip dots was located on the nose at 5% of the model length to enable the laminar-to-turbulent transition of the surface flow. The trip dots are 0.29 mm tall, have a diameter of 1.27 mm, and are spaced 2.54 mm apart (centre-to-centre). The measurements were conducted at axial stations, $x/L =$ 0.45 and 0.65 as shown in Fig. 1.

The measured axial pressure distribution from Manovski et al. (2020) over the studied geometry is shown in Fig. 1, where U_∞ is the incoming freestream velocity. Herein, x denotes the streamwise direction, y the spanwise direction (out of the page), and z the vertical direction. The pressure coefficient, $C_p = \Delta P/0.5\rho U_\infty^2$, where ΔP is the difference between the local surface static pressure and the pressure within the settling chamber, and ρ is the air density. The measurement uncertainty for C_p is less than 2%. A varying pressure distribution exists, including a near ZPG over the mid-body at $x/L = 0.3$–0.6 with $C_p \lesssim -0.067$, followed by a mild FPG at $x/L = 0.6$–0.7. Then, an adverse pressure gradient (APG) exists in the tail at $x/L \gtrsim 0.8$, which is stronger with axial distance.

A key parameter used for TBL analysis is the friction velocity (U_τ). This study presents a unique implementation of oil film interferometry (OFI), detailed in the supplementary documentation S2, to directly measure the skin friction on the surface of the axisymmetric model and obtain an

accurate estimate of U_τ. These values are listed in Table 3 for the measurement locations.

3 Measurement techniques

3.1 Time-resolved particle image velocimetry

Two-dimensional TR-PIV was undertaken with tracer particles (di-ethyl-hexyl-sebacate, DEHS) from a six-jet TSI seed generator (model *9306*). Illumination was provided by a InnoLas Nanio Air 532-10-V-SP high-speed laser and a Phantom v2640 high-speed camera imaged particles. The laser and camera synchronisation was provided by a LaVision PTU X. The displacement of particles in sub-regions, or interrogation windows (*IW*), was determined by cross-correlation PIV software (LaVision Davis 10.2). The laser light sheet was aligned along the streamwise direction with the camera orthogonal to the laser sheet, therefore allowing the measurement of instantaneous streamwise (u) and wall-normal (w) velocity components.

The InnoLas Nanio Air laser is an air-cooled Nd:YVO_4 diode-pumped solid-state laser with 532-nm wavelength and a typical operating repetition range of 20–80 kHz. The laser has a maximum pulse energy of approximately 550 μJ per pulse at 20 kHz, which is considerably smaller than ≈ 150 mJ pulse energies typical of dual-cavity PIV lasers used for large field-of-view or high-resolution setups as in (Manovski et al. 2020). At 40 kHz, the pulse energy reduces to ≈ 310 μJ, whereas at 80 kHz, it is ≈ 140 μJ. The laser pulse width is 18 ns and 30 ns for 40 kHz and 80 kHz, respectively, all of which are adequate to 'freeze' the motion of particles for a typical PIV image magnification (Scharnowski and Kähler 2020). To maintain sufficient laser energy for PIV, the light sheet of the high-speed laser was limited to a narrow strip, approximately $7 \times 55\,\mathrm{mm}^2$, in the streamwise and wall-normal directions. This size strip was produced by a cylindrical lens of −400 mm focal length. Additionally, two spherical lenses of 1.5 m and 1.0 m focal length were placed in series to focus the laser sheet to a minimal waist.

The InnoLas high-speed single-cavity laser used here offers benefits over dual-cavity PIV lasers, such as consistent pulse energy and uniform illumination without beam overlap issues. Dual-cavity systems allow flexible time separation between pulses to match local flow velocities, while the single-cavity laser in this study was operated at a fixed repetition frequency, setting the pulse separation as $\Delta t = 1/f$, where f is the repetition rate. Maximum particle displacement was estimated based on freestream velocity, laser rate and image magnification. While larger Δt improves dynamic range and reduces statistical uncertainty, it risks bias errors from flow acceleration, curved streamlines, and particle loss from the *IW* or light sheet (Scharnowski and Kähler 2020).

High spatial resolution is critical in PIV to resolve turbulent flow scales, especially in thin boundary layers. Here, a large focal length lens provided the required magnification, though fixed laser frequencies and Δt increased pixel displacement and particle density requirements. For this study, a 24.62 px/mm magnification was chosen to enable analysis of temporal resolution effects at consistent spatial resolution. This magnification was achieved, from a stand-off distance of 1.4 m, using a large focal length lens, Nikon AF-S 400-mm G f2.8 lens with an in-house actuated aperture control mechanism as described in Manovski et al. (2020). With this optical setup, the imaged particles typically ranged in size from 2 to 3 pixels, which is within the optimal range for PIV measurements (Scharnowski and Kähler 2020).

The range of acquisition rates in this study was from 40 kHz to 80 kHz, with camera limitations requiring a cropped image width in the x-direction of 224 px and 144 px, respectively. The z-direction or wall-normal image resolution remained constant at 1664 px. The 400-mm lens was operated at $f_\#$ (ratio of lens focal length to aperture diameter) of 2.8 to enable strong particle image signals. The camera on-board RAM (288 GB) allowed 500,000 to 800,000 samples to be collected over 12.5 s and 10 s, for 40 kHz and 80 kHz, respectively. The experimental parameters for the TR-PIV are summarised in Table 1 at the measured axial locations. The total acquisition length in seconds of the TR-PIV sequence at each station is given by T. The non-dimensional boundary layer turnovers can be calculated using outer scaling, TU_e/δ, where δ is the boundary layer thickness when the streamwise mean flow is 99% of the edge freestream velocity (U_e). The number of boundary layer turnovers must be sufficiently large, typically $\mathcal{O}(10^4)$, to ensure sufficient statistical convergence of the largest length scale in the energy spectra.

PIV processing was performed by DaVis 10.2 and consisted of an initial size (IW_1) of 64 px × 64 px and 50% overlap. A final *IW* size (24 px × 24 px) was then chosen and shifted by the displacement estimated in the first pass, with image deformation and three iterative passes to ensure better convergence of the cross-correlation peak (Scarano 2001). The spatial resolution of the TR-PIV in each direction is represented by SR_x, SR_y and SR_z, as detailed in Table 1. Vector validation and identification of spurious vectors were performed after each pass using a neighbourhood (5 × 5 vector) median filter with 2 px tolerance. Iterative linear interpolation was then used to fill any holes left by the validation process. Filling holes enables continuous velocity data time series, which is essential for conducting spectral analysis. The percentage of spurious vectors was, on average, less than 1% of the total vectors. Peak locking was assessed through the analysis of particle displacement histograms and was not apparent.

In the case of 2D PIV, spatial averaging occurs in all three dimensions. In-plane, the two finite dimensions of the *IW* can be accurately established using the image calibration. Accurately measuring the laser sheet thickness is typically challenging for the out-of-plane dimension. Using sensitive burn paper, the laser sheet thickness (ls_t) was found to be 2 mm by measuring the extremities of the laser burn. The laser beam diameter is commonly defined as either full-width half maximum (FWHM) or $1/e^2$, corresponding to the width at 13.5% of the peak intensity. By taking the optical setup and the laser beam properties, a theoretical laser sheet thickness can also be estimated based on thin lens theory (Saleh and Teich 2019). For our optical setup and manufacturer specified laser-quality factor, $M^2 = 1.2$, the estimated waist thickness is 0.64 mm ($1/e^2$) and 0.37 mm (FWHM). Direct methods to quantify the thickness, such as using a laser beam profiler (Grayson et al. 2017) or traversing a knife edge across an energy metre (Mullin and Dahm 2005), offer greater accuracy than the burn paper method, but were not available for this study. In 2D PIV, the Gaussian laser profile results in a varying intensity distribution, such that the imaged particles also exhibit a varying intensity throughout the measurement volume. Depending on each imaged particle's size and image intensity, its weighting to the PIV cross-correlation function within the *IW* will vary. Furthermore, between snapshots, variations in particle concentrations and light intensity throughout the laser sheet plane are likely. Although the later case is minimal in our setup due to the use of single-cavity laser, an open question remains, in the context of 2D PIV and out-of-plane spatial averaging, how representative is the laser sheet thickness obtained from these various means? The ensemble-averaged PIV should contain a combination of all of the above effects. By using a reliable, highly resolved reference measurement (in this case hot-wire) and applying the spatial filtering to TBL DNS data that matches the TR-PIV spatial resolution, it is possible to determine an effective laser sheet thickness (ls_e) for the PIV measurements at hand. This approach is detailed in Sect.5.2.

3.2 Particle tracking velocimetry from particle image velocimetry

For the PTV from PIV, the particles are initially identified based on a specified particle size range (1.5 px to 4 px) and an intensity threshold of 40 counts. The results from the TR-PIV are then used as a predictor (or particle shift correction) for subsequent frames to guide the particle tracking and match particle pairs within a 2 px tolerance. Once matched particle pairs are found, a *IW* (4 px × 4 px) is centred around each resulting position. Individual particle correlations between frames then determine a more accurate particle shift (and velocity) for each particle pair. The scattered particle tracks are then interpolated on a regular grid using an ensemble bin-averaging approach (Manovski et al. 2021). A very small bin size (2 px × 2 px, $\approx 7^+ \times 7^+$ in the x and z directions) and high-resolution statistical quantities were then obtained due to the large number of snapshots, while ensuring sufficient statistical convergence within each bin. The PTV measurement parameters for the two axial locations are summarised in Table 1. While spatial spectra can be obtained over particle tracks from PTV, the limited streamwise extent of the measurement restricted the ability to obtain reliable spectral content over a sufficiently broad range of scales. Additionally, fine-scale interpolation of PTV data to a regular grid for spectral analysis is a potential approach, but was constrained by the low particle track density, which limits the accuracy of the reconstructed velocity fields. Hence, PIV data with a uniform grid are better suited for spectral analysis.

3.3 Hot-wire anemometry

The work by Hutchins et al. (2009) established a series of requirements for hot-wire measurements to minimise the attenuation of turbulence levels due to the spatial and temporal averaging in wall-bounded flows. They recommend that the viscous scaled hot-wire active length (l^+) should be as small as possible, with errors found when $l^+ > 20$. These errors significantly reduced with distance from the wall and were minimal in the outer layer (outside the log region) for $l^+ < 79$ at $Re_\tau \approx 14000$. Additionally, Hutchins et al. (2009) recommended that the length-to-diameter (l/d) ratio of the wire should be ≥200 to minimise attenuation due to end conduction effects. Regarding temporal resolution, they recommend the viscous timescale ($t_c^+ = t_c U_\tau^2/\nu$) should be less than 3, where t_c is the time resolution of the measurement taking into account the Nyquist cut-off frequency. This study uses highly resolved hot-wire measurements with a 1.5-µm-diameter wire, an active length of 0.37 mm and were acquired at $f_a = 80$ kHz, resulting in $l^+ = 29$ and $t_c^+ \approx 2.4$, thereby satisfying the general requirements of Hutchins et al. (2009). Additionally, hot-wire measurements which were less resolved ($l^+ \approx 95$) were repeated and acquired at 40 kHz in order to better understand the effects of spatial and temporal resolution. The active wire length in both cases was measured before and after testing using a Nikon Shuttlepix PM-MFSC microscope. The measurement post-testing was to ensure that the dimensions and the integrity of the wire were maintained. For the hot-wire measurements, the corresponding antialiasing low-pass filter was set to the Nyquist frequency cut-off value ($f_c = f_a/2$). For each case, 35 points were taken with logarithmic spacing using a wall-normal traverse with an acquisition period (T) of 30 s per data point. In order to accurately determine the wind-on probe tip position relative to the wall and to correct for the small amount (< 0.05 mm = 4 wall units) of backlash in the traverse

system, the probe tip was imaged using a high-resolution camera (29 Mpx) fitted with a 300 mm lens and 3× teleconverter. The key hot-wire measurement parameters are presented in Table 1. The remaining hot-wire setup, including the calibration procedure, follows the same process detailed in Manovski et al. (2020).

To ascertain the frequency response of the hot-wire anemometer, an input square wave response was analysed using the 'Bode' plot method. For the 1.5-µm wire, a typical frequency response of 30 kHz was found. Hutchins et al. (2015) outline that the actual frequency response may be less than that derived from this method, but still provides a useful ballpark indication. Hutchins et al. (2015) present a method to quantify frequency response using a pressurised facility to keep *Re* constant while varying the frequency content, but this approach is impractical for most researchers due to limited access to such facilities and variations in hot-wire tuning (e.g. under-damped vs. over-damped setups). The paper provides useful examples of potential frequency responses that could be encountered in hot-wire experiments. For example, for a typical 5-µm wire, the expected frequency response is flat up to 5–7 kHz. Hence, for measurements in turbulent flows with considerable energy above these frequencies, the frequency response of hot-wire may cause large errors in measurement quantities. As indicated by Hutchins et al. smaller sensors help and provide faster frequency response as is the case here with the reduction in both spanwise length (1.22 mm vs 0.37 mm) and diameter (5 µm vs 1.5 µm). Furthermore, Hutchins et al. state that the error due to frequency response for wall-bounded flows will be minimal if the ratio of U_τ^2/ν is below $0.3 \times 10^5\ s^{-1}$ with errors becoming significant above $2 \times 10^5\ s^{-1}$. In our case, this ratio is slightly above the recommended ratio, at around $1 \times 10^5\ s^{-1}$. The performance of our hot-wire measurements is verified by comparisons with fully resolved DNS at matched conditions, in Sects. 5.2 and 5.3.

4 TR-PIV: theoretical cut-off frequencies

The cut-off frequency for TR-PIV is the frequency beyond which the PIV system can no longer reliably capture the flow's velocity fluctuations. This is when the signal significantly attenuates or where noise dominates, making the measurements unreliable. The cut-off frequency represents the highest frequency at which the PIV system can provide accurate fluctuations of the velocity. Frequencies higher than the cut-off are either not captured or attenuated, leading to an incomplete or inaccurate flow representation. Below we consider three separate theoretical TR-PIV cut-off frequencies. There are additional cut-off frequencies (or wavelengths) due to the three-dimensional (3D) spatial averaging of the PIV method and its inherent noise, which can be determined from the frequency response and the spectral content of the PIV measurement with reference to a highly reliable or ground truth spectral dataset. This will be explored in Sect. 5.3 and 5.5.

4.1 Temporal acquisition cut-off frequency

The temporal acquisition cut-off frequency, f_c, is determined directly by the acquisition frequency (f_a), following the Nyquist criterion: $f_c = f_a/2$.

4.2 Tracer particle cut-off frequency

Depending on the size and density of the tracer particles, they will follow the fluctuating velocity of the flow up to a certain cut-off frequency (f_p). Typically, PIV has a low-pass filtering behaviour due to the high particle-to-fluid density ratio. Following Mei (1996), an estimate of f_p can be found for a particle diameter based on a particle dynamic equation. The analysis is based on theoretical assumptions, where a prescribed velocity oscillation determines the cut-off frequency. It is based on a velocity-squared difference between the oscillation and resulting particle lag of 50% (equivalent to a -3 dB threshold).

For the DEHS seed generator used in this study, a complementary test was undertaken in which in situ particle sizing was conducted for the same imaging setup and is described in Manovski et al. (2022a). The measurements from two particle sizers were combined to cover a particle diameter range of 0.1 µm to 3 µm. The DEHS geometric median of the volumetric concentration was found to be 0.62 µm. In the literature, the reported mean diameter of DEHS aerosol particles from a Laskin nozzle is 0.5–1.5 µm (Raffel et al. 2018), while a commonly reported geometric median diameter is 1 µm (Kähler et al. 2002).

An alternative approach used in transonic/supersonic flows is to calculate the particle response time (τ_p) from the exponential decay of ensemble-averaged PIV data across a shock wave, from which an effective particle size can be determined (Manovski et al. 2022a). This effective diameter contains the holistic effects of the PIV system. For DEHS generated from a PIVTEC *PIVpart 45* seed generator equipped with 12 Laskin nozzles, $\tau_p = 1.92$–2.02 µs was reported across shock waves by Ragni et al. (2011). As a point of reference, for $\tau_p = 2$ µs and for the test conditions and optical setup given in Ragni et al. (2011), the corresponding effective particle size of DEHS can be calculated to be 0.82 µm.

In the particle size and response tests of Manovski et al. (2022a), both water and oil-based smoke particles were also sized, revealing a geometric median diameter of 0.3–0.35 µm, whereas the effective particle diameters derived from particle response tests were found to range

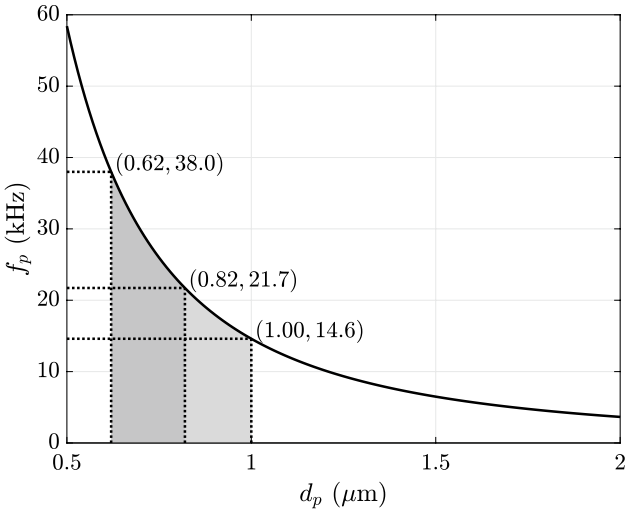

Fig. 3 The particle size and density-dependent cut-off frequency (f_p) and particle diameters (d_p) based on Mei (1996) theoretical assumptions. The shaded area indicates the range of particle cut-off frequencies for the expected size of particles within this study

between 0.70 and 0.85 µm. This size discrepancy was attributed to the light scattering properties of the small particles and a correlation bias favouring larger particles in PIV processing. Larger particles contribute more to the cross-correlation peak, while smaller particles, not imaged effectively, scatter less light and predominantly contribute to background noise. This finding underscores the limitation that particle sizer tests alone do not fully reflect the characteristics of imaged particles undergoing PIV processing.

Following the analysis of Mei (1996), for DEHS (with density = 912 kg/m^3) the particle cut-off frequencies are as shown in Fig. 3. Using the measured particle sizer median diameter of 0.62 µm as a lower limit, the effective diameter of 0.82 µm from Ragni et al. (2011), and 1 µm as an upper limit, we get the shaded area indicating the particle cut-off frequencies (f_p = 14.6 – 38.0 kHz) for the range of expected particle diameters (d_p = 0.62 –1.00 µm).

To accurately track the flow without significant particle lag, the Stokes number (St)—defined as the ratio of the particle response time to the timescale of the flow—should be below 0.1 to maintain slip velocity errors of less than 1% (Samimy and Lele 1991). Using τ_p = 2 µs for DEHS particles from Ragni et al. (2011) (d_p = 0.82 µm, f_p = 21.7 kHz) and a viscous time limit of $t_c^+ = 3$ (Hutchins et al. 2009) to capture the smallest timescales within the TBL, we obtain $St = 0.07$. Using the measured value of d_p = 0.62 µm (f_p = 38 kHz) and an estimated τ_p = 1.3 µs based on the Stokes drag formulation, we find $St = 0.04$, which is well below the benchmark of 0.1. These results suggest that the tracer particles used here effectively follow the turbulent structures with minimal slip velocity (i.e. lag) error.

Table 1 The hot-wire, TR-PIV and PTV measurement parameters for the range of measurement locations. The spatial resolution of each technique in each direction is represented by SR_x, SR_y and SR_z

Hot-wire														
x/L	U_e (m/s)	U_τ (m/s)	Re_τ	$SR_x = d$ (µm)	$SR_x^+ = d^+$	$SR_y = l$ (mm)	$SR_y^+ = l^+$	$SR_z = d$ (µm)	$SR_z^+ = d^+$	f_a (kHz)	f_c (kHz)	t_c^+	T (s)	TU_e/δ
0.45	29.8	1.19	1025	5.0	0.4	1.17	95	5.0	0.4	40	20	4.7	30	7×10^4
0.45	29.8	1.19	1025	1.5	0.1	0.37	29	1.5	0.1	80	40	2.4	30	7×10^4
0.65	30.7	1.22	1424	5.0	0.4	1.17	99	5.0	0.4	40	20	4.7	30	7×10^4
0.65	30.7	1.22	1424	1.5	0.1	0.37	30	1.5	0.1	80	40	2.4	30	7×10^4
TR-PIV														
x/L	U_e (m/s)	U_τ (m/s)	Re_τ	$SR_x = IW$ (mm)	$SR_x^+ = IW^+$	$SR_y = ls_e$ (mm)	$SR_y^+ = ls_e^+$	$SR_z = IW$ (mm)	$SR_z^+ = IW^+$	f_a (kHz)	f_c (kHz)	t_c^+	T (s)	TU_e/δ
0.45	29.7	1.19	1040	0.97	79	0.8±0.2	65±15	0.97	79	80	40	6.8	10	2×10^4
0.65	30.3	1.21	1470	0.97	80	0.8±0.2	68±15	0.97	80	80	40	6.8	10	2×10^4
PTV														
x/L	U_e (m/s)	U_τ (m/s)	Re_τ	SR_x (mm)	SR_x^+	$SR_y = ls_e$ (mm)	$SR_y^+ = ls_e^+$	SR_z (mm)	SR_z^+	f_a (kHz)	f_c (kHz)	t_c^+	T (s)	TU_e/δ
0.45	29.7	1.19	1045	0.08	7	0.8±0.2	65±15	0.08	7	80	40	6.8	10	2×10^4
0.65	30.3	1.21	1470	0.08	7	0.8±0.2	66±15	0.08	7	80	40	6.8	10	2×10^4

4.3 Spatial resolution cut-off frequency

For PIV, the smallest resolvable length scale can be related to the velocity fluctuations limited by the size of the *IW*. The finite *IW* size imposes additional temporal filtering, over Δt, on the dataset. In wall-bounded shear flows, the highest spatial resolvable frequency, $f_{\max}$, is dependent on the PIV system spatial resolution and can be estimated by considering the ratio of the smallest resolved length scale, $L_{\min}$, to the convection velocity of turbulent scales in the streamwise direction, U_c, within the measurement volume. In the case of 2D planar PIV measurements, the measurement volume is defined as the laser sheet thickness within the *IW*. Given a convection velocity, U_c, and the smallest resolved length scale, $L_{\min}$, the maximum resolvable frequency, $f_{\max}$, can be expressed as,

$$f_{\max} \approx \frac{U_c}{L_{\min}}. \tag{1}$$

Following Willert and Gharib (1991), the spatial cut-off wavelength is twice the *IW* size, according to the Nyquist criterion. Schrijer and Scarano (2008) and Schneiders et al. (2018) also state that a spatial modulation up to 50% of the velocity fluctuation is achieved when $L_{\min} = 2\times IW$. The minimum resolvable length can therefore be approximated as twice the *IW* size, and therefore the highest resolvable frequency of velocity fluctuations is equivalent to the spatial cut-off frequency and is given by

$$f_{\max} \approx \frac{U_c}{2 \times IW}. \tag{2}$$

In wall-bounded shear flows, different scales within the measurement volume are convected at varying speeds. For a representative maximum, we take the local freestream (or edge) velocity (U_e) as the convection velocity, leading to $f_{\max} \approx U_e/(2 \times IW)$.

Willert (2015) also analysed the spatial resolution cut-off frequencies for TR-PIV in a TBL. Willert considered a finite *IW* streamwise size and used the mean velocity at a wall-normal location, $U(z)$ as the corresponding convection velocity, from which an effective sample time is defined as:

$$t_{IW} = \frac{IW}{U(z)}. \tag{3}$$

Accordingly, it follows that the highest resolvable frequency or spatial cut-off frequency, while taking into account the Nyquist criterion, is given by

$$f_{IW} = \frac{1}{t_{IW}} = \frac{U(z)}{2 \times IW}. \tag{4}$$

If the local freestream velocity (U_e) is used as the mean velocity for an upper limit of the spatial cut-off frequency, Eq.(2) and Eq.(4) are equivalent.

It should be noted that iterative processing with image deformation can alter the effective *IW* size and shape, particularly in regions with strong velocity gradients or high shear. This deformation process may affect the relationship between pixel dimensions and actual spatial resolution, making it challenging to accurately estimate the spatial cut-off frequency. Furthermore, the above analysis did not account for the influence of the spanwise spatial resolution, which is constrained by the laser sheet thickness. In a TBL, the spanwise direction plays a crucial role due to the anisotropy of turbulence and the presence of smaller structures and steep gradients in this direction. In the case of Willert (2015), the reported laser sheet thickness was 0.2 mm (2.7 wall units); as such, the effects of the spanwise direction on f_{IW} were negligible. However, that is not the case in the present investigation. The impact of the full 3D spatially filtering effect of TR-PIV on turbulence statistics and spectral response is assessed in Sect. 5.2 and 5.3. Furthermore, we derive a transfer function between the TR-PIV and DNS spectra by using DNS (or hot-wire) data as a reference. This allows us to establish new spatial cut-off wavelengths that account for the combined effects of spatial resolution and inherent PIV measurement noise. These findings are detailed in Sect. 5.5.

5 Test results

5.1 Mean velocity and streamwise Reynolds stress

The cross-validation with hot-wire and DNS is made at axial stations, $x/L = 0.45$ and 0.65. The boundary layer parameters at these two stations are summarised in Table 3, derived by averaging the results from the hot-wire and TR-PIV measurements. The mean boundary layer parameters were obtained using the experimental data, with any missing data near the wall supplemented by fitting data to functions as detailed in Manovski et al. (2020) for the inner wall and the logarithmic law of the wall. At $x/L = 0.45$, the boundary layer flow exhibits a near ZPG ($dP/dx \approx -0.4$ Pa/m) with the Clauser pressure gradient parameter, $\beta = -0.001$, Whereas, at $x/L = 0.65$, the boundary layer flow exhibits a small FPG ($dP/dx \approx -158$ Pa/m) with $\beta = -0.247$. Since the curvature parameter which is defined as the ratio of the boundary layer thickness, δ, to the radius of curvature, $a = 133.9$ mm, is small (i.e. $\delta/a \ll \mathcal{O}(1)$) and a^+ is large ($\gtrsim 200$), the flow at these locations should follow the canonical flat plate solution (Piquet and Patel 1999; Kumar and Mahesh 2018; Manovski et al. 2020). Here, we defined the boundary layer thickness, δ, at the location of the mean streamwise velocity approaches 99% the local freestream

velocity (i.e. $U = 0.99U_e$). The measured boundary layer data are compared with canonical flat plate DNS of Sillero et al. (2013). For the DNS, the TBL and simulation parameters are summarised in Tables 2 and 3, respectively. The flow conditions for the DNS indicate only a small mismatch with our data. The number of DNS grid points in each direction is indicated by N_x, N_y and N_z, and T_s is the total time over which statistics are compiled. At $x/L = 0.65$, the measured boundary layer data are also compared with the DNS of Sillero et al. (2013). Although the flow conditions at this location differ, the comparison of turbulent statistics remains valuable since the flow parameters are quite similar and the FPG is mild, minimising significant deviations.

In Fig. 4a and b, the normalised mean streamwise velocity profiles ($U^+(z) = U(z)/U_\tau$) as a function of the normalised wall-normal height, $z^+ = zU_\tau/\nu$, are plotted for the TR-PIV and the two hot-wire measurements as well as the DNS datasets. The law-of-the-wall, $U^+ = z^+$, and the logarithmic law, $U^+ = \kappa^{-1}\log z^+ + A$, are also included to Fig. 4a and b for comparison. Here $\kappa = 0.41$ and $A = 5.0$ are the logarithmic law constants. In Fig. 4, the vertical dash-dotted lines at $z^+ = 200, 400$ and 600 indicate the location of extracted spectra and will be discussed in Sect. 5.2. The mean streamwise velocity for the TR-PIV datasets is averaged in time (t) and streamwise (x) extent of the measurement domain at each z-location, while for the hot-wire signal U is obtained from averaging the signal in t at each z-location. At both axial locations, the mean profiles from all methods compare reasonably well and follow the logarithmic law-of-the-wall profile. In the near-wall buffer region, the lower-resolution hot-wire cannot resolve the flow gradients and suffers from heat loss, resulting in a departure from the inner viscous wall relationship. At $x/L = 0.65$, Fig. 4b, owing to the mild FPG compared to the ZPG DNS, there is a small contraction of the outer wake profile which is due to acceleration of the local flow.

In Fig. 4c and d, the normalised streamwise Reynolds stresses ($uu^+ = \langle uu\rangle/U_\tau^2$) are plotted for the various test methods and the DNS datasets for the ZPG and APG cases. An under-prediction of the turbulence levels is obtained compared to the DNS, particularly in the region closer to the wall ($z^+ < 600$) and can be attributed to the spatial averaging inherent in each method. The highly resolved hot-wire (with $l^+ = 29$) can better resolve the turbulence levels, as the measured levels tend towards the DNS data. The next best performer is the larger hot-wire, followed by the TR-PIV. The relative disparity between methods is consistent across the two axial locations. This confirms that inadequate spatial resolution attenuates the measured turbulence levels in a TBL over an axisymmetric body of revolution, with attenuation increasing closer to the wall and with lower spatial resolution, as noted by Chin et al. (2009) in a turbulent channel flow. In the next section, the DNS is spatially filtered to verify the effects of spatial resolution.

Table 2 The DNS simulation parameters (Sillero et al. 2013) for the two cases that match the TR-PIV test conditions at measurement locations, $x/L = 0.45$ and 0.65. The spatial resolution in wall units of the DNS in each direction is represented by SR_x^+, SR_y^+ and SR_z^+

DNS										
case	U_e (m/s)	Re_τ (m/s)	Re_θ	N_x	$SR_x^+ = \Delta x^+$	N_y	$SR_y^+ = \Delta y^+$	N_z	$SR_z^+ = \Delta z^+$	$T_s U_e/\delta$
DNS_a	1.0	1040	2996	1284	7	4096	3.8	200	3	673
DNS_b	1.0	1307	4000	1284	7	4096	3.8	200	3	708

Table 3 Boundary layer parameters at the axial measurement locations compared with DNS dataset (Sillero et al. 2013)

Measurement location	x/L	0.45	DNS_a	0.65	DNS_b
Friction velocity	U_τ (m/s)	1.19	–	1.21	–
Boundary layer thick	δ (mm)	12.82	–	17.23	–
Displacement thick	δ^* (mm)	2.18	–	2.71	–
Momentum thick	θ (mm)	1.56	–	2.00	–
Shape factor	$H = \delta^*/\theta$	1.40	1.38	1.35	1.38
Friction coefficient	$C_f = 2U_\tau^2/U_e^2$	0.00319	0.00328	0.00319	0.00342
Momentum Re	$Re_\theta = U_e\theta/\nu$	3163	2996	4076	4000
Friction Re	$Re_\tau = U_\tau\delta/\nu$	1045	1040	1470	1307
Pressure coefficient	$C_p = \Delta P/0.5\rho U_\infty^2$	−0.067	0	−0.102	0
Pressure gradient	dP/dx (Pa/m)	−0.4	0	−158	0
Clauser pressure gradient	$\beta = \delta^*/\tau_w(dP/dx)$	−0.001	0	−0.247	0
Curvature parameter	δ/a	0.10	–	0.13	–
Radius in wall units	$a^+ = aU_\tau/\nu$	1.1×10^4	–	1.1×10^4	–

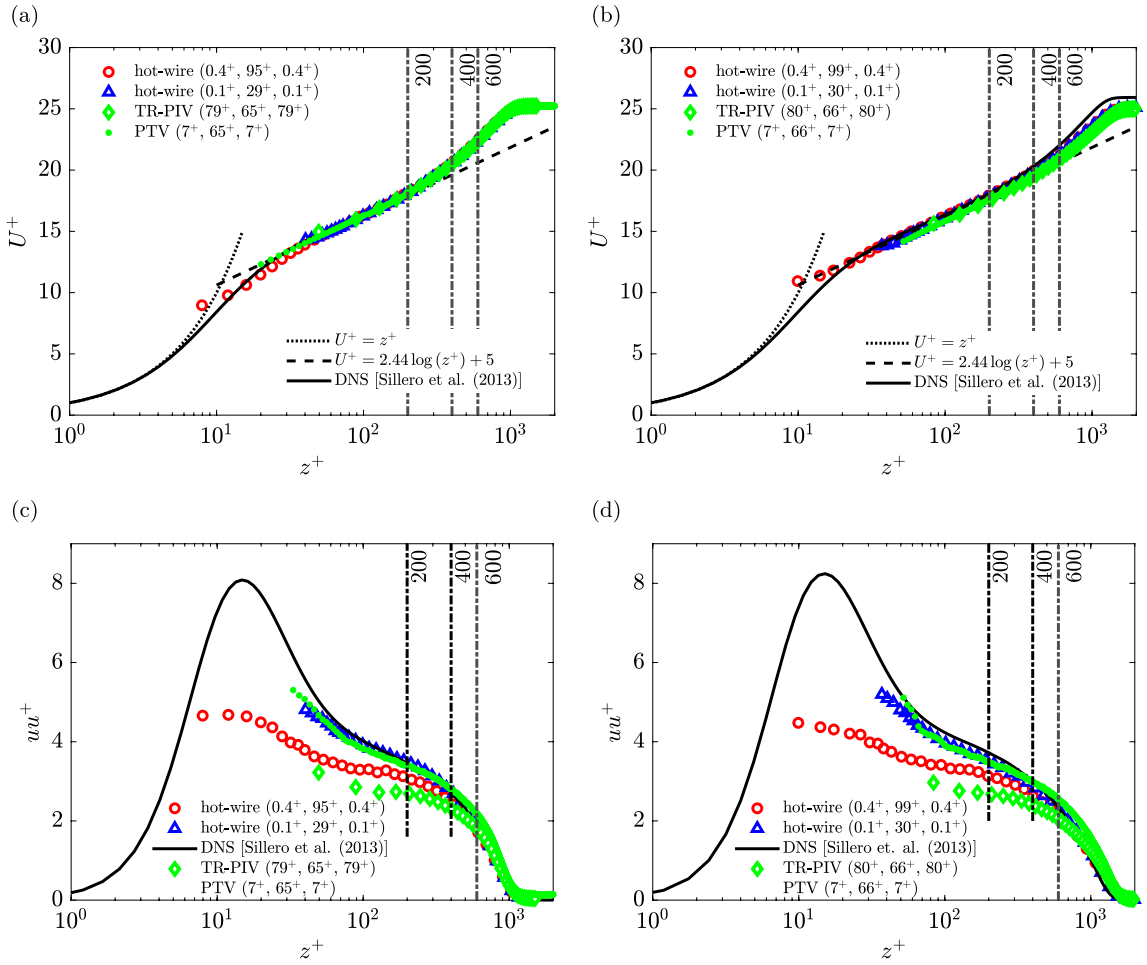

Fig. 4 Non-dimensional mean streamwise velocity profiles U^+ (a, b) and non-dimensional mean streamwise Reynolds stress uu^+ (c, d) as a function of wall-normal distance, at axial locations, $x/L = 0.45$ (a, c) and 0.65 (b, d), compared for the different test methods and DNS. The spatial resolution of each method in each direction is indicated in the parentheses as (x^+, y^+, z^+). The dotted and dashed lines are the law-of-the-wall $U^+ = z^+$ and log-law $U^+ = \kappa^{-1} \log z^+ + A$. The vertical dash-dotted lines at $z^+ = 200, 400$ and 600 are the location of extracted spectra and will be discussed in Sect. 5.2

The PTV results are also shown in Fig. 4. The bin size for the PTV was 2 px (≈ 7 wall units) in the x- and z-directions, and the number of samples in each bin was greater than 8,000. The PTV can match the mean velocity profiles and recover the turbulence levels almost at the same level of the small hot-wire. The PTV results also verify the effects of spatial resolution and the subsequent reduction in turbulence attenuation. The impact of spanwise resolution ($SR_y = 65 - 66^+$), influenced by laser sheet thickness, is less pronounced as PTV measures individual particle fluctuations, typically tracking the brightest particles near the laser sheet's centre. Although the out-of-plane velocity component could introduce slight errors, this effect is considered negligible at these locations and over the small Δt. One limitation of PTV is the absence of rigorous validation criteria, which may result in spurious particle track connections, potentially inflating turbulence levels—similar to the noise observed in PIV studies by Atkinson et al. (2013). Despite this, the PTV results suggest that the individual particle displacements are reliable, indicating there is little inherent bias error in the TR-PIV imaging.

5.2 Comparisons with spatially filtered DNS

The DNS data from Sillero et al. (2013) were filtered using a volumetric spatial boxcar filter to simulate the spatial resolution of the PIV and hot-wire measurements. This filtering method enables direct comparison of turbulence statistics. The details of the filtering process are provided in the supplementary material (S3).

The results for the streamwise and wall-normal Reynolds stress are presented in Fig. 5 with uncertainty bounds and the corresponding spatially filtered resolution indicated in the parentheses as (x^+, y^+, z^+). The uncertainty quantification

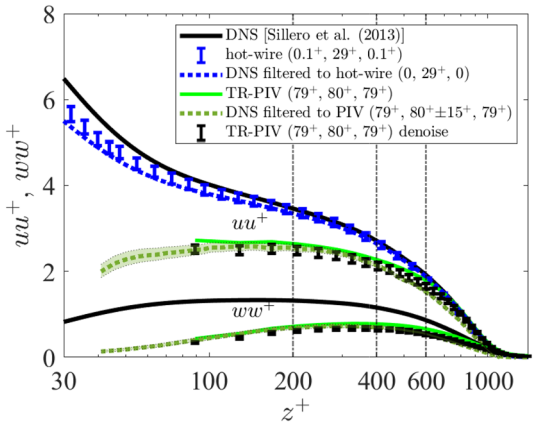

Fig. 5 At $x/L = 0.45$, hot-wire and TR-PIV normalised mean Reynolds stress profiles in the streamwise, uu^+, and wall-normal components, ww^+ as a function of wall-normal distance (z^+), compared with DNS of Schlatter and Örlü (2010), and spatially filtered DNS matching the hot-wire and TR-PIV resolutions. The spatial resolution of each method in each direction is indicated in the parentheses as (x^+, y^+, z^+)

is presented in Appendix C and takes into account the main contributors to the uncertainty of each method. For the streamwise mean velocity, the estimated uncertainty of the hot-wire was ~ 0.8% (relative to U_e), and an uncertainty of ~ 0.20% was found for the TR-PIV. For the Reynolds stresses, the maximum estimated uncertainty for the hot-wire and TR-PIV was ~ 2.5% and ~ 3.9%, respectively. Referring to Fig. 5, a comparison between the hot-wire and the spatially filtered DNS matching the hot-wire (7^+, 29^+, 5^+) shows that most differences fall within the uncertainty bounds of the hot-wire measurements, as indicated by the blue error bars, with only a slight overestimation observed. This minor discrepancy may stem from the effective sensing length of the hot-wire (as discussed in S3) and the underlying DNS spatial resolution in the streamwise direction (7^+) and the interpolated wall-normal direction (5^+), which are absent in the hot-wire measurements. The results confirm that the turbulence levels at this location over the axisymmetric body of revolution geometry match very closely with a canonical TBL.

As discussed earlier for PIV, the in-plane spatial resolution is approximated by the finite *IW* size and can be established from the TR-PIV processing settings. To estimate the effective laser sheet thickness (ls_e) in the TR-PIV measurements, we use a filtering approach applied to the DNS data. Specifically, we adjusted the spanwise filter size of the DNS until the spatially filtered Reynolds stress profiles from the DNS visually matched those obtained from the TR-PIV measurements. The effective laser sheet thickness is identified as the spanwise filter size that provides the closest match between the TR-PIV and filtered DNS Reynolds stress profiles. It is assumed to remain consistent across all measurement stations. Using this method, the DNS filtered to TR-PIV (79^+, $65^+ \pm 15^+$, 79^+) profile in Fig. 5 is obtained, indicating $ls_e^+ = 65 \pm 15$ (0.8 ± 0.2 mm), which is significantly less than the 2 mm thickness observed by the burn test and larger than the estimated thin lens thicknesses of 0.64 mm ($1/e^2$) and 0.37 mm (FWHM). The uncertainty bounds on ls_e^+ were set to match the estimated uncertainty of the TR-PIV.

In Fig. 5 the wall-normal Reynolds stress ($ww^+ = \langle ww \rangle / U_\tau^2$) results show the expected attenuation and also fall within the spatially filtered profile and the uncertainty bounds. It should be noted that in Fig. 5, both the raw and denoised TR-PIV results (denoised through filtering methods described in Sect.5.4) are presented. The differences between the two profiles are minimal, with the denoised data showing slightly lower turbulence levels, representing an optimised case for the TR-PIV. Consequently, the denoised data were used to determine ls_e. In the outer-layer portion of the boundary layer ($z^+ \approx 600$ or 0.5δ), the difference between the DNS and the measured streamwise Reynolds stresses from the hot-wire and TR-PIV was similar (with a maximum error of ≈ 3%), which is within the range of measurement uncertainty. This is a significant finding, as it suggests that the TR-PIV in this study can be considered reliable for capturing the outer TBL flow. However, it is essential to examine the spectral response across a range of scales for both the TR-PIV and hot-wire measurements, which is discussed in the following section.

5.3 TR-PIV: spectral response

A range of temporal and spatial scales of motion characterises turbulent flows. The power-spectral densities (PSD or spectra) of the velocity fluctuations, $\Phi(f)$, can be used to determine the relative contribution of different frequencies to the overall energy content. In our study, the streamwise velocity fluctuation spectra (Φ_{uu}) were calculated using the modified periodogram method of Welch with a Hamming window and 50% overlap. For the TR-PIV, two fast Fourier transform (FFT) window sizes of 2^9 and 2^{12} were used, and the results were combined to obtain better converged low- and high-frequency spectra. The frequency resolution for the two window sizes was ≈ 137 Hz and ≈ 17 Hz, respectively. These frequencies normalised using outer boundary layer scales, result in non-dimensional frequencies, $f_e = f\delta/U_e = 0.060$ and 0.007, respectively. The spectra from the TR-PIV are also averaged at each wall height across the streamwise domain (typically over 12–16 vectors).

We again use the DNS from Sillero et al. (2013) and the spatially filtered DNS dataset as a reference. For each spanwise location, spatial spectra along the streamwise direction were computed and then averaged across all spanwise locations. A final average was then calculated

across the available 13 time independent DNS snapshots. Using the filtered DNS spectra as a reference, we can directly assess the spectral (or frequency) response of the TR-PIV and hot-wire results, evaluating the ability to capture the flow dynamics across various scales and frequencies, thereby determining the range of resolvable flow scales.

The premultiplied energy spectra, $k_x\Phi_{uu}$ (where k_x is the streamwise wavenumber and Φ_{uu} is the energy spectrum of the streamwise velocity fluctuations), plotted against the streamwise wavelength (λ_x^+), are presented in Fig. 6. The results include all measurement methods at both axial stations, along with the original and spatially filtered DNS data. For $x/L = 0.45$, the DNS results are used as the reference,

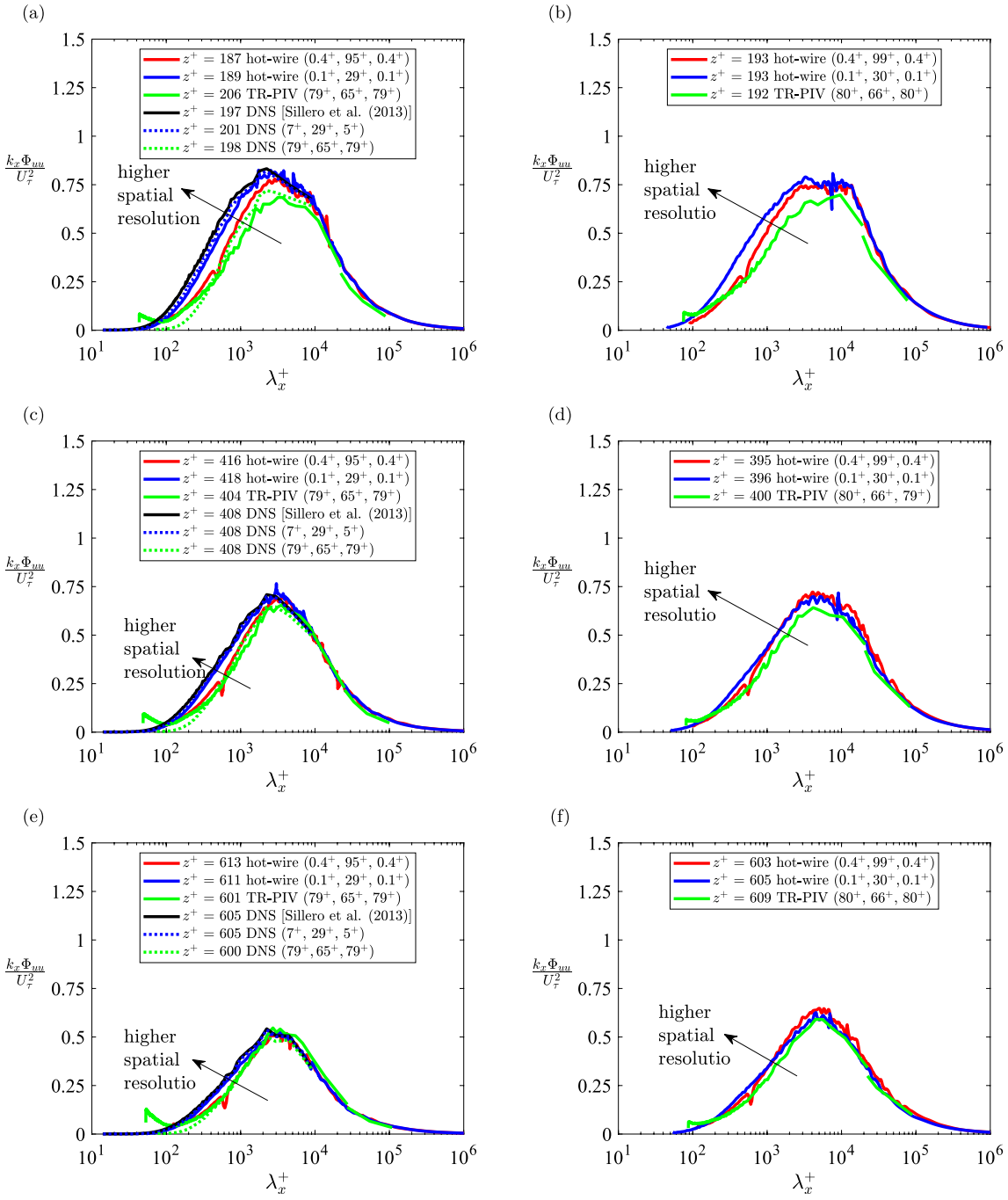

Fig. 6 At axial locations, $x/L = 0.45$ (left) and 0.65 (right), the non-dimensional premultiplied energy spectra of the streamwise velocity fluctuations compared with different methods at three wall heights, $z^+ \approx 200$ (a, b), 400 (c, d), and 600 (e, f). For each method, the corresponding spatial resolution in each direction is indicated in the parentheses as (x^+, y^+, z^+)

while at $x/L = 0.65$, the DNS dataset is excluded due to the presence of the FPG. Given the spectral differences between pressure gradient cases, as demonstrated in Appendix A, the hot-wire measurements are used as the reference at this location. The corresponding filtered resolution in each direction (x^+, y^+, z^+) is indicated for each method. The spectra are presented at three wall-normal heights of $z^+ \approx 200$ (which is in the logarithmic region), $z^+ \approx 400$ (end of the logarithmic region), and $z^+ \approx 600$ ($0.4\delta - 0.5\delta$, in the outer wake region). The vertical lines in the previous figures of the mean velocity and Reynolds stress profiles indicate these three wall heights. The k_x and λ_x were obtained from the time-series data by applying Taylor's frozen turbulence hypothesis and taking the local mean velocity as the convection velocity. The maximum uncertainty in the spectra is determined in Appendix C and was found to be ± 5.0% for the TR-PIV and ± 2.9% for the hot-wire, occurring in the large scales ($\lambda_x^+ \approx 20 \times 10^3$) near the peak in energy content. The energy distribution from the streamwise fluctuations exhibits a broadband character, with the shape of the spectrum consistent with flat plate DNS results across all methods. As we move towards larger scales, the DNS spectra terminate abruptly, reflecting the limited spatial extent of the extracted dataset and the inability to resolve the largest structures. Nevertheless, the influence of these larger scales remains evident in the data, given that the full DNS streamwise domain is approximately 12 times larger. For the hot-wire and TR-PIV spectra, applying Taylor's hypothesis and having sufficient temporal data allow us to resolve these large scales. In Fig. 6 an arrow indicates the direction of higher spatial resolution. At both axial locations, the lower-resolution measurements show a noticeable disparity in the range of scales that can be resolved, with the degree of attenuation increasing as the distance to the wall decreases. Notably, the peak energy levels are not fully captured by the TR-PIV at the first two wall heights. However, at $z^+ = 600$ (Fig. 6 e, f), the peak levels are well captured by all methods, indicating a lower sensitivity to spatial resolution effects at this higher wall-normal position. The peak values are consistently captured from then onward to the edge of the boundary layer (not shown).

At $z^+ \approx 400$ (Fig. 6c, d), for both axial locations, the profiles of each method compare reasonably well for $\lambda_x^+ \gtrsim 3000$, below this wavelength there are signs of spatial attenuation. The smaller hot-wire (0.1^+, $29–30^+$, 0.1^+) offers the best resolution and a result closest to the DNS, next best is the large hot-wire (0.4^+, $95–99^+$, 0.4^+), whereas the TR-PIV has the largest attenuation. Further away from the surface ($z^+ \approx 600$, Fig. 6e, f), the influence of small-scale energy reduces, the effect of spatial resolution becomes less pronounced, and all methods agree fairly well. This trend continues for increasing wall heights (not shown), in which all the measurement methods are able to fully resolve the dominant wavelength scales. It should be noted, at $z^+ \approx 600$, the difference between the DNS and the measured streamwise Reynolds stress from the hot-wire and TR-PIV is below 3%.

The spectral response of the spatially filtered DNS results at $x/L = 0.45$ is also shown in Fig. 6. The dotted spectra depict the expected output of the hot-wire and TR-PIV in the absence of measurement noise. We observe that the small hot-wire demonstrates a consistent response across the full range of broadband scales, closely aligning with the corresponding profile of the spatially filtered DNS. In contrast, the TR-PIV data reveal a distinct "kick-up" or roll up in the smaller wavelength scales when compared to the spatially filtered DNS results. This kick-up is indicative of the presence of small-scale (high-frequency) noise, a low-pass filtering effect that has been previously documented by Foucaut et al. (2004), Atkinson et al. (2013), Willert (2015), Squire et al. (2016), Beresh (2021). In the direction of decreasing length scale, after the kick-up, the spectral energy levels reach a local minimum before rising again with decreasing scales. This local minimum signifies the onset of a form of TR-PIV aliasing (Beresh 2021), where it appears that the unresolved small-scale components of the flow are improperly mapped to smaller scales, thereby contaminating the TR-PIV results. The small-scale noise underscores the limitations of TR-PIV in accurately capturing the full spectrum of turbulence at these smaller scales. Despite this, the overall effects of the small-scale noise on the streamwise Reynolds stress are minimal, as seen in Fig. 5, with only a marginal increase in turbulence levels compared with the equivalent noise-free spatially filtered DNS and the denoised TR-PIV (see Sect. 5.4 for details). A similar trend is observed at $x/L = 0.65$, although the influence of the small-scale TR-PIV noise appears to be lower as the kick-up is less severe. This disparity between the two axial locations and pressure gradients is the subject of further discussion in Appendix A.

Given the presence of small-scale noise in the TR-PIV data, it is prudent to address these limitations and strive to improve the accuracy of the turbulence measurements. Fortunately, with the reference DNS dataset, we can explore filtering or denoising methods to mitigate this noise. The effectiveness of these filtering techniques and their impact on the spectral response of the TR-PIV results are discussed in the following section.

5.4 TR-PIV: effective filtering

The anisotropic denoising using the uncertainty quantification method of Wieneke (2017) was used to filter the TR-PIV. The method provides an optimal trade-off between smoothing strength and truncation error. This is done by locally adapting the spatial filter size based on whether neighbouring vectors fall within or outside an uncertainty threshold. This approach results in smoother results while

keeping the spatial resolution high. It has been successfully applied to various flow fields, including jet flow, ring vortex and turbulent pipe flow (Wieneke 2017), and can potentially be applied to separated or highly unsteady flows with appropriate adjustments. We use a weak smoothing strength of 2.5 that acts as a multiplier on the uncertainty threshold, limiting the maximum filter size and producing a smaller spatial kernel size with less smooth vectors. An initial spatial filter size of 7×7 vectors was used, which then varies depending on the local uncertainty quantification. After the spatial filtering, a temporal Gaussian filter of a width equal to 5 time steps is applied. At $x/L = 0.45$ we can assess the effectiveness of the denoising filter by comparing directly with the spatially filtered (noise-free) DNS of matching TR-PIV resolution. In Fig. 7a, c, the results are shown again at two wall heights, for $z^+ \approx 200$ and 600. We see that the denoising filter performs well, as shown by the two profiles exhibiting good overlap across the full range of wavelength scales. The denoised results do not exhibit the "kick-up" evident in the TR-PIV small scales, and instead, at these small scales, we observe a consistent offset to the fully resolved DNS. Cut-off wavelengths corresponding to the *IW* and $2 \times IW$ sizes, as well as -3 dB and -1 dB thresholds, are also shown in Fig. 7 and will be discussed in the following section.

At the downstream axial location (Fig. 7b, d), due to the FPG, the hot-wire is used as the reference and the results are plotted for the TR-PIV with the denoising filter. The denoising filter is seen to perform well, as indicated by a near-constant offset with the reference hot-wire results, over the range of scales and the two wall-normal heights.

To quantitatively compare the effectiveness of the denoising filter, we plot the transfer function ($|TF|$), as the square root of the ratio of the spectra from the denoised filter ($\Phi_{uu[\mathrm{TR-PIV}]}$) with the spatially filtered DNS ($\Phi_{uu[\mathrm{DNS_{TR-PIV}}]}$) in Fig. 8. An ideal filter would exhibit a flat response with $|TF| = 1$ across all scales. In our data, we observe a relatively flat response, remaining close to unity, across most scales, ($\lambda_x^+ \gtrsim 400$), and wall-normal heights. For small scales $\lambda_x^+ < 400$, we observe a sharp decline following a slight hump. This hump is more pronounced closer to the wall,

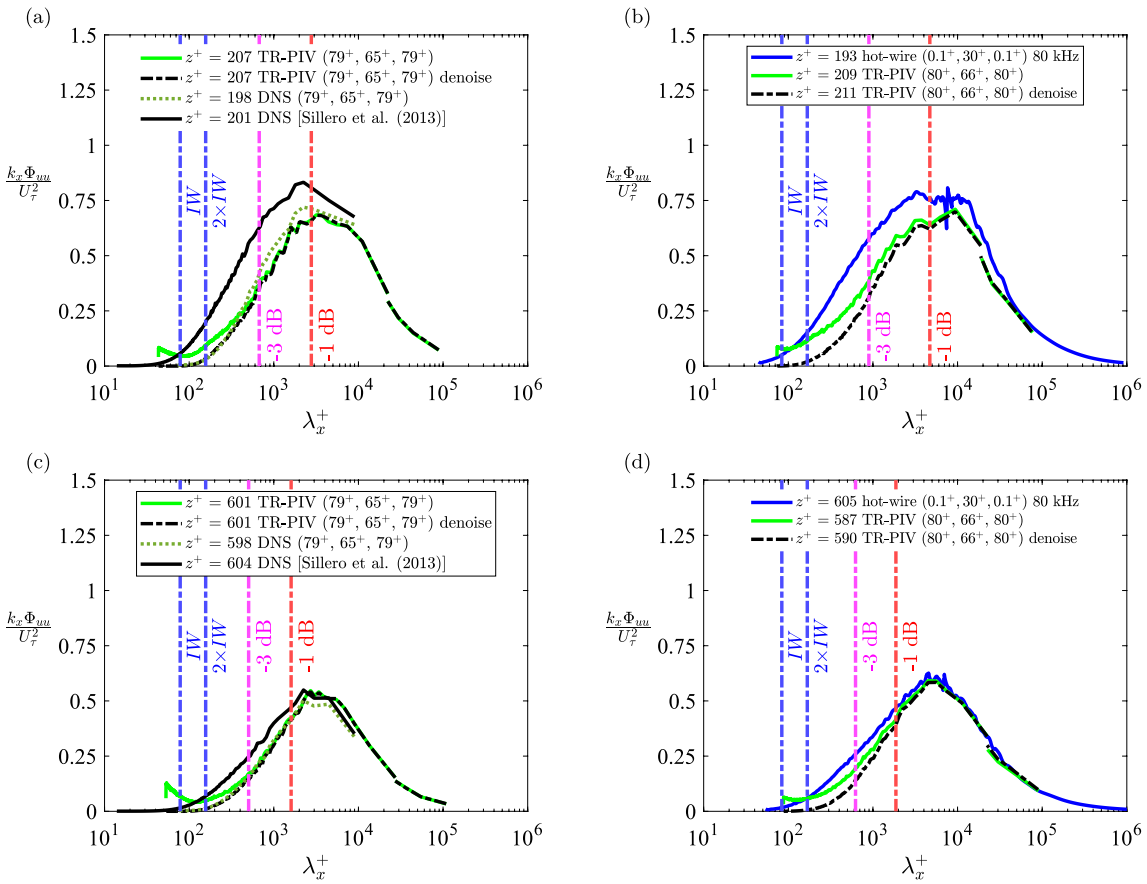

Fig. 7 Comparison of raw and denoised TR-PIV results at axial locations $x/L = 0.45$ (left) and 0.65 (right), of the non-dimensional premultiplied energy spectra of the streamwise velocity fluctuation at two wall heights, $z^+ \approx 200$ (**a**, **b**) and 600 (**c**, **d**). The spectra are benchmarked against DNS from Sillero et al. (2013) and spatially filtered DNS matching TR-PIV resolution. Cut-off wavelengths are indicated by dashed-dotted lines, with *IW* and $2 \times IW$ in blue, -3 dB in magenta and -1 dB in red

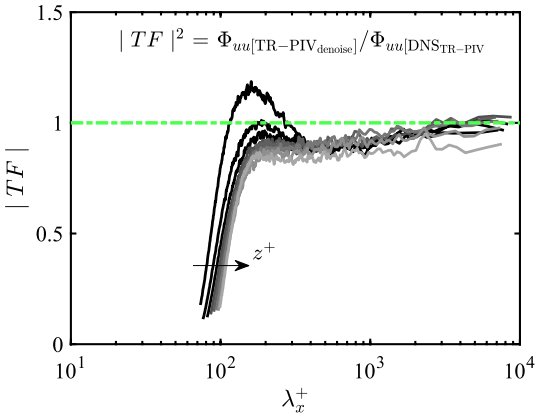

Fig. 8 Transfer function of the denoised TR-PIV energy spectra of the streamwise velocity fluctuations with the spatially filtered noise-free DNS spectra, matching the TR-PIV resolution as a function λ_x^+. The lighter shading indicates increasing wall-normal distance, ranging from $z^+ \approx 100$ to 1100

where the strength of small scales is stronger. Furthermore, a larger deviation from unity is observed near the edge of the boundary layer (lightest shade of grey). At this location, the magnitude of $|TF|$ is highly sensitive to small discrepancies between the two energy spectra, as their absolute values are lower. The observed discrepancy near the boundary layer edge may result from the propagation of minor errors in determining the wall position and friction velocity. Additionally, it could be influenced by slight mismatches in the friction velocity.

5.5 TR-PIV: cut-off wavelengths

To assess the spectral response and establish suitable spatial cut-off wavelengths for the TR-PIV data across various wavelengths and wall heights, we compute the 1D transfer function, $|TF|$, which can be determined from the 1D spectra following:

$$|TF| = \sqrt{\frac{\Phi_{uu[\text{TR-PIV}]}}{\Phi_{uu[\text{DNS}]}}} = \text{TR-PIV/DNS}, \tag{5}$$

where $\Phi_{uu[\text{TR-PIV}]}$ and $\Phi_{uu[\text{DNS}]}$ are the streamwise velocity spectra of the TR-PIV and full-resolution DNS, respectively. It is important to note that these transfer function calculations differ from those in Fig. 8, as we now compare the TR-PIV results to the full-resolution DNS. We also calculate $|TF|$ for the denoised TR-PIV results relative to the DNS dataset, denoted as "TR-PIV$_{\text{denoise}}$/DNS" in the text and figures. For $x/L = 0.65$, we use the hot-wire results as the reference spectrum (denominator value in Eq. (5)) and refer to this transfer function as "TR-PIV$_{\text{denoise}}$/hot-wire" throughout the text and figures.

The cut-off wavelength (or frequency) can be defined from the transfer function by identifying the wavelength at which the amplitude of the spectral signal drops below a specific threshold. A commonly used threshold for low-pass filters is -3 dB, which corresponds to a 50% relative difference at each wavelength (or frequency) and is often referred to as the half-power threshold. This approach was adopted by Atkinson et al. (2013) for PIV spectral analysis, as PIV effectively acts as a low-pass filter. We deem that a 50% relative difference at each wavelength is considerable. Therefore, in this study, we propose a more stringent threshold corresponding to a 20% relative difference, equivalent to a -1 dB threshold. This more conservative approach is intended to provide a more precise interpretation of the spectral data and better determine the resolvable scale limits in TR-PIV measurements, which is particularly important when analysing small-scale turbulent structures.

The $|TF|$ profiles for different wall heights are presented in Fig. 9, along with the cut-off wavelength thresholds of -1 dB and -3 dB for both axial locations, and for the raw and denoised TR-PIV data. Starting from the large scales and moving towards smaller scales, the raw TR-PIV data initially resolve the larger scales effectively with $|TF| \approx 1$. However, as we transition to smaller scales, the TR-PIV data fall below the defined thresholds, with this drop-off occurring sooner in measurements taken closer to the wall. As the wavelength decreases further, the $|TF|$ reaches a local minimum before rising again, a behaviour attributed to the previously discussed "kick-up" and aliasing effect in the TR-PIV data. Notably, due to the "kick-up" present at both axial locations, the raw TR-PIV barely crosses the -3 dB threshold. For the denoised TR-PIV data, the local minimum is eliminated and the $|TF|$ continues its downward trajectory without the same resurgence. Additionally, it is interesting to note that the spread of profiles between near-wall and outer-layer measurements is greater for the ZPG case than for the FPG case. This observation is explored in more detail in Appendix A.

When the transfer function profile intersects either of the two cut-off thresholds (shown in Fig. 7 for $z^+ \approx 200$ and 600), the corresponding wavelength is identified and extracted for each wall height profile. For the raw TR-PIV data, where the thresholds are crossed twice, the more restrictive, larger wavelengths were selected. In Fig. 7, in the absence of reference spectra, one may infer that the minimum resolvable TR-PIV scale is indicated by the location of local minima or the onset of aliasing in the spectral profiles. These local minima correspond to spatial scales between IW and $2 \times IW$, varying slightly by wall height. Notably, $2 \times IW$ was previously identified as the theoretical spatial resolution cut-off wavelength in Sect. 4.3. However, with the availability of reference spectra, we observe that the TR-PIV spectra attenuate small scales and exhibit a roll-off at considerably

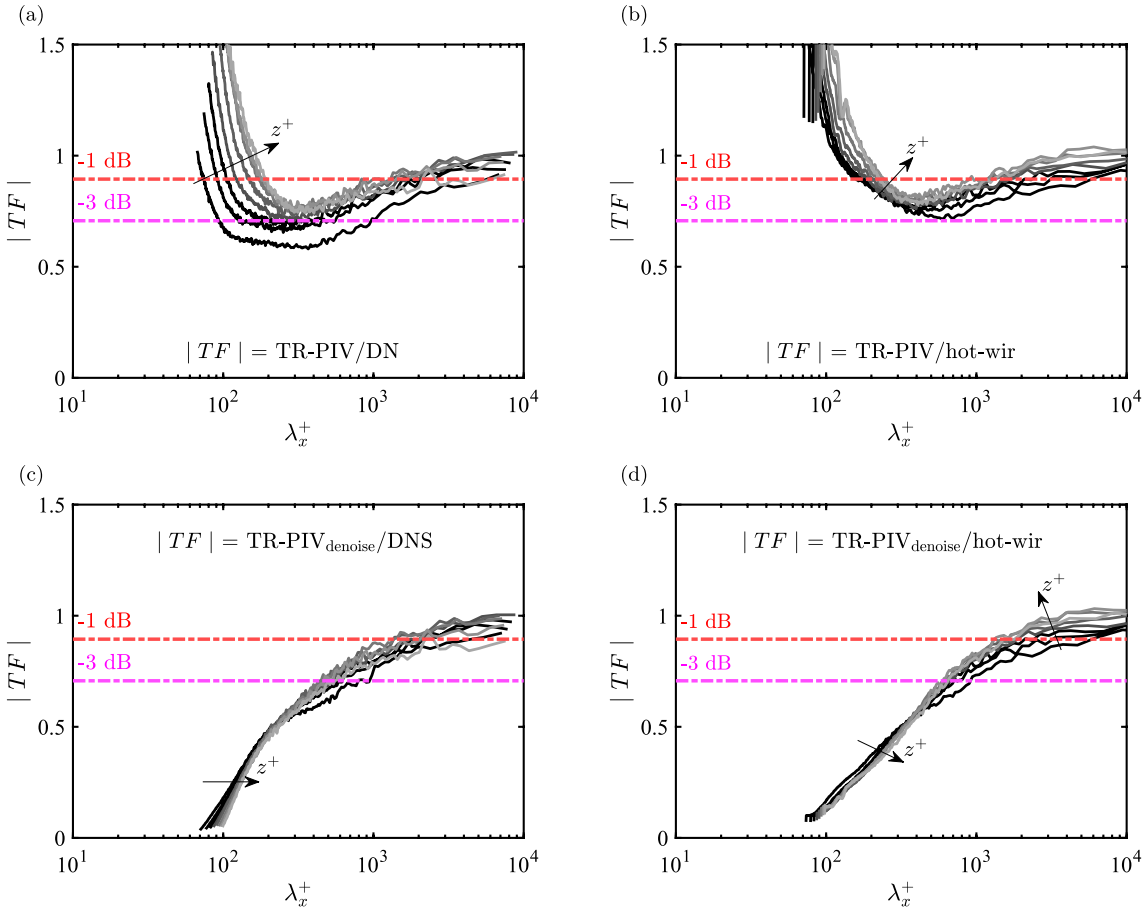

Fig. 9 At axial locations, $x/L = 0.45$ (left) and 0.65 (right), the transfer function of the TR-PIV energy spectra of the streamwise velocity fluctuations with the DNS spectra (**a**) as a function of wavelength. Transfer function of the TR-PIV spectra with the hot-wire spectra (**b**). Transfer function of the denoised TR-PIV spectra with the DNS spectra (**c**). Transfer function of the denoised TR-PIV spectra with the hot-wire spectra (**d**). The dash-dot horizontal lines indicate the -1 dB (red) and -3 dB (magenta) cut-off wavelength thresholds. The lighter shading indicates increasing wall-normal distance, ranging from $z^+ \approx 100$ to 1100

larger scales, where the -1 dB and -3 dB thresholds provide a more accurate indication of the minimum resolvable scales.

The resultant -1 dB and -3 dB cut-off wavelengths across the boundary layer are plotted in Fig. 10a for the ZPG location. This figure shows the normalised premultiplied 1D energy spectrograms of the streamwise velocity fluctuations from the TR-PIV as a function of the wall-normal distance for different wavelength scales. The spectrograms are scaled by inner ($^+$) and outer (δ) scales, whereas in Fig. 10 (b), the same spectra are replotted as a function of dimensionless timescales (t^+) and frequencies (f). The small gap in each contour plot is due to the interface between the large and small window lengths used to calculate the spectra from the TR-PIV. In the two figures, we also include an overlay of spectral energy isobars (in cyan) for the reference case, i.e. DNS of Sillero et al. (2013). The red dotted lines indicate cut-off wavelengths for the raw TR-PIV for the -1 dB threshold, with reference to the DNS, while the solid red and magenta lines indicate the cut-off wavelengths, again with reference to the DNS spectra of the denoised TR-PIV. The dashed red and magenta lines indicate the ideal cut-off wavelengths for the (noise-free) spatially filtered DNS that match the resolution of the TR-PIV and indicate the absolute best result that one would expect from a filter removing all the inherent PIV noise, while only the effects of spatial resolution remain. These cut-off wavelength lines mark the threshold beyond which significant attenuation occurs in the TR-PIV measurements. A clear negative slope is observed across raw, denoised and idealised cut-off wavelengths as the distance from the wall increases. This trend confirms that smaller scales become increasingly resolvable with greater wall height, primarily due to the reduced contribution of small scales to the overall energy content at these heights. In contrast, the inherent TR-PIV noise (the "kick-up") significantly affects the cut-offs in the raw TR-PIV data. As a result, the dotted red curves exhibit larger cut-off wavelengths closer to the wall. The denoised TR-PIV results show slightly higher cut-off values than the idealised

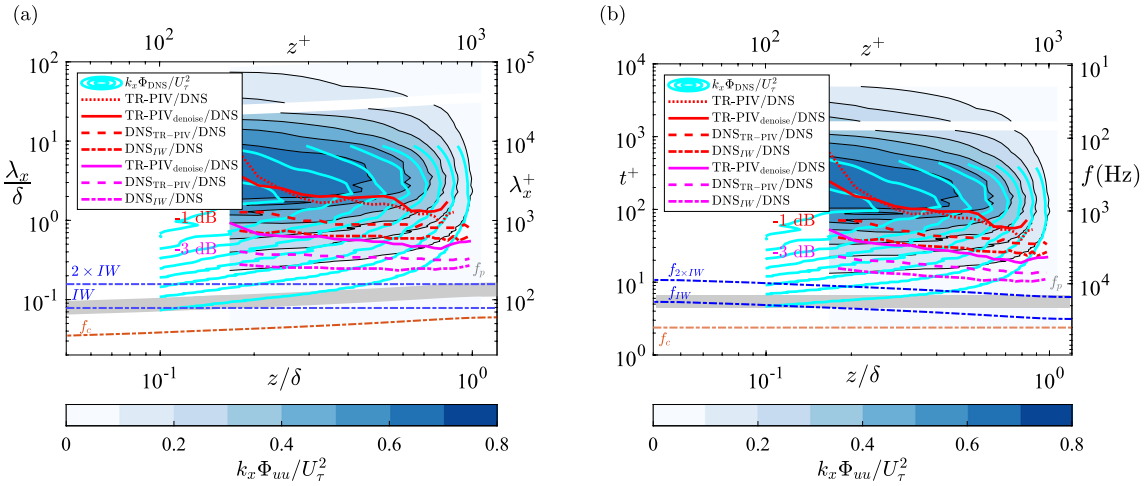

Fig. 10 At $x/L = 0.45$, **a** the non-dimensional premultiplied energy spectra of the streamwise velocity fluctuations from the denoised TR-PIV as a function of the wall-normal distance for different wavelength scales. **b** The same spectrogram is plotted as a function of viscous timescales and frequencies. Various cut-off wavelengths (and frequencies) are indicated for -1 dB (red) and -3 dB (magenta) thresholds and were calculated from *TF* profiles using the DNS as the reference. Theoretical derived, acquisition (f_c, dash-dotted orange line), particle (f_p, grey shading) and spatial resolution cut-off wavelengths (*IW*, dash-dotted blue line) and frequencies (f_{IW}, dash-dotted blue line) are also shown. Reference energy spectral isobars from the DNS (Sillero et al. 2013) are displayed in cyan

noise-free DNS cut-offs, suggesting that there is still room for filter optimisation.

As another idealised case, we also show the cut-off wavelength and frequencies, labelled DNS$_{IW}$ and indicated by dash-dot red and magenta lines in Fig. 10. This is the case of spatially filtered DNS matching only the *IW* size in x- and z-directions, representing the case if the laser sheet thickness and inherent TR-PIV noise were negligible.

Comparing the isobars of the TR-PIV with DNS reference spectra, we see a similar shape and the expected attenuation in the small scales. The isobars of the TR-PIV are offset slightly by up to a quarter of a contour level ($k_x\Phi_{uu}/U_\tau^2 \approx 0.25$). This is especially apparent closer to the wall and for the larger scales ($\lambda_x^+ \gtrsim 50 \times 10^3$) and is largely a consequence of the limited spatial extent of the DNS data. The large-scale structures are truncated, resulting in poor spectral convergence due to the limited spatial domain of the dataset. The hot-wire spectra do not suffer from such an effect, and consequently, we see a favourable match with the TR-PIV spectra over the larger scales at both axial locations, as shown in Fig. 11 where the hot-wire spectra are plotted as a reference. It is also important to highlight that the spatial spectra derived from DNS represent a direct measurement. In contrast, TR-PIV and hot-wire measurements rely on Taylor's frozen turbulence hypothesis to determine the spatial wavelengths and wavenumbers and assume that convection velocities are equivalent to the local mean flow. Accounting for the scale-dependent convection velocities may yield slightly different spectral isobars, as shown by (de Kat and Ganapathisubramani 2015; Renard and Deck 2015). TR-PIV, with its combined temporal and spatial range, provides the necessary data to obtain scale-dependent convection velocity and is the subject of further study.

It should be noted that the same methodology, which includes comparisons with DNS for mean and Reynolds stress profiles, assessment of the spectral response and determination of the cut-off wavelengths, was applied to various TR-PIV processing settings. These settings included different final *IW* sizes (16 px, 24 px, 32 px), *IW* shapes (square, circular and elliptical), as well as different *IW* overlaps (0%, 50% and 75%). Although the results of this analysis are not shown here, the best-performing settings were selected as a compromise between spatial resolution and inherent noise. The optimal configuration was determined to be a final *IW* size of 24 px, a circular shape, and 50% overlap. Atkinson et al. (2015) explored the use of Gaussian spatial filters (3×3 and 5×5, in the x- and z-directions) in combination with an 11-point temporal filter to match PIV data with spatially filtered DNS. While these filters were effective, variations of them were also tested in this study and found to be less suitable compared to the anisotropic denoising method applied here. The latter was superior, as it provided a more accurate spectral response and better preserved the small-scale turbulence.

In the spectrogram plots of Figs. 10 and 11, we also indicate the theoretical cut-off wavelengths and frequencies associated with the temporal, particle and spatial resolution, as determined in Sect. 4. Also, we include as an absolute upper limit for the theoretical spatial resolution cut-offs (*IW* and f_{IW}), which represents the smallest wavelength, $L_{\min} = IW$. For the particle cut-off (f_p), we display the shaded area representing the particle size range shown in Fig. 3. For the

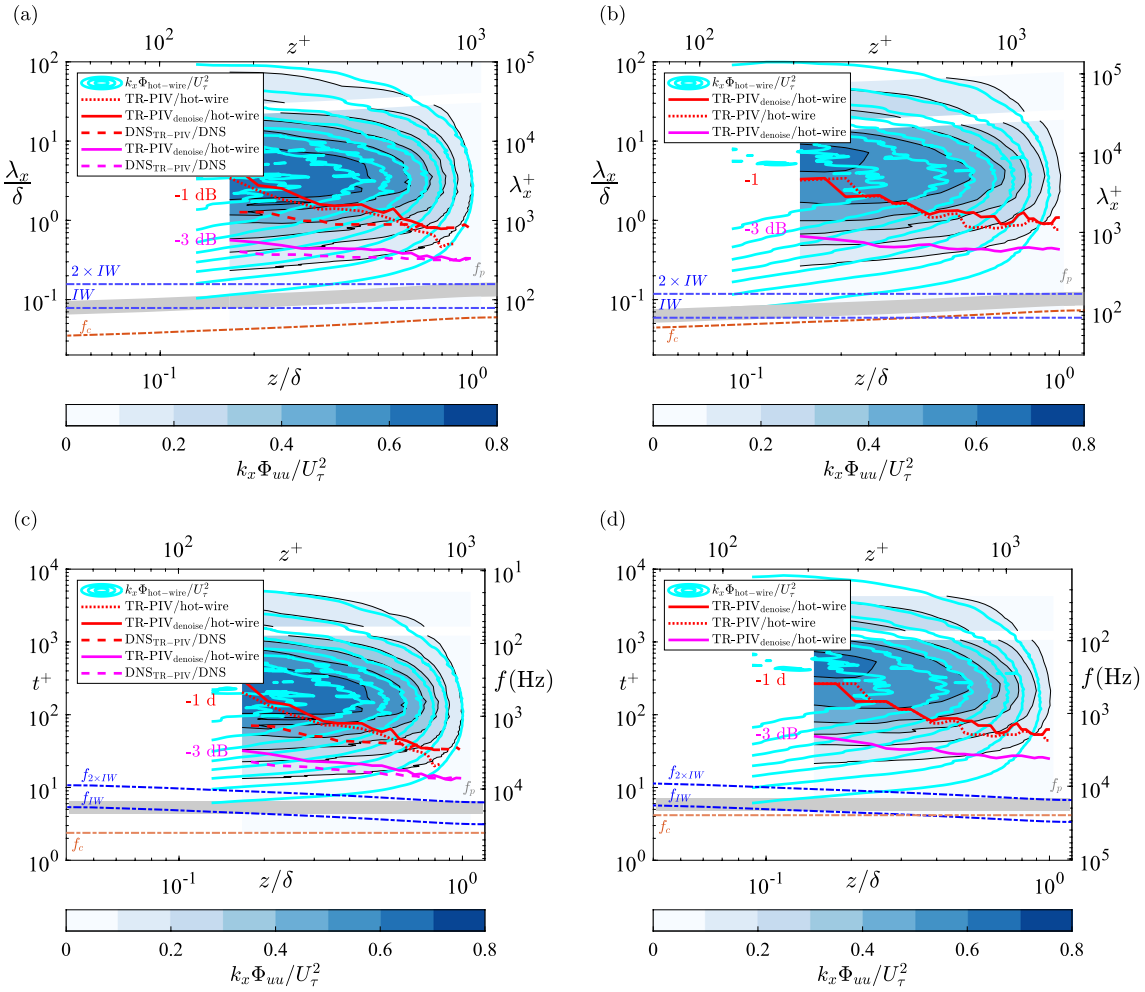

Fig. 11 At axial locations, $x/L = 0.45$ (left) and 0.65 (right), normalised premultiplied 1D energy spectrograms of the streamwise velocity fluctuations from the denoised TR-PIV as a function of the wall-normal distance for different wavelength scales in (**a**) and (**b**). The same spectrograms are plotted as a function of viscous timescales and frequencies in (**c**) and (**d**). For both the raw and denoised TR-PIV, cut-off wavelengths (and frequencies) are indicated for -1 dB (red) and -3 dB (magenta) thresholds, calculated from *TF* profiles using the hot-wire results as the reference. The idealised noise-free DNS wavelength cut-offs, from *TF* profiles using the fully resolved DNS as a reference, are also shown and are represented by the dashed red and magenta lines in (a) and (c). Theoretical derived, acquisition (f_c, dash-dotted orange line), particle (f_p, grey shading) and spatial resolution cut-off wavelengths (*IW*, dash-dotted blue line) and frequencies (f_{IW}, dash-dotted blue line) are also shown. Reference energy spectral isobars from the hot-wire are displayed in cyan

most part, the majority of the energy content lies outside these limits, indicating that they do not significantly impact measurement accuracy. However, it is important to note that the spatial resolution cut-offs ($2 \times IW$ and $f_{2\times IW}$, represented by the dash-dot blue lines) result in a substantial underestimation, as they do not account for the spanwise averaging effects introduced by the laser sheet thickness and any inherent TR-PIV noise. Furthermore, as previously highlighted, these theoretical limits may not accurately represent the effective spatial resolution due to *IW* deformation, variations in particle distribution and local flow gradients within the *IW*. Even when assuming a negligible laser sheet thickness, the corresponding spatially filtered DNS cut-offs (labelled "DNS$_{IW}$/DNS" and represented by the dash-dotted red and magenta lines) are considerably larger than the theoretical spatial resolution limits.

While the temporal resolution or acquisition frequency appears sufficient to capture the energy content of the flow in the outer layer, the spatial resolution proved to be the limiting factor. In particular, the measurement's spatial resolution significantly constrained the ability to resolve small scales closer to the wall.

In Fig. 11, similar spectrogram plots are shown for the ZPG location (left) and FPG location (right); except this time, the small hot-wire spectra measurements (shown in cyan colour) are used as the reference to determine the -1 dB

and -3 dB cut-off wavelengths from the corresponding transfer functions. In these plots, we observe that the large scales of the reference spectra match well with the TR-PIV isobars. We see the expected attenuation in the TR-PIV in the small scales (and high frequencies). The new cut-off wavelengths and frequencies for the TR-PIV relative to the hot-wire results are shown in the same fashion as in Fig. 10. We observe a similar negative trend in the cut-off wavelengths. However, the slope is steeper as the outer layer is better represented in the hot-wire results compared with the canonical DNS, which was constrained by the limited streamwise spatial extent used to compute the DNS spectra. For the ZPG case, we also plot the cut-off wavelengths and frequencies for the idealised noise-free spatially filtered DNS matching the resolution of the TR-PIV using the fully resolved DNS as a reference. These cut-offs, labelled "$\mathrm{DNS_{TR\text{-}PIV}/DNS}$", are again shown by the dashed red and magenta lines. In the outer layer, the new -1 dB and -3dB cut-offs for the denoised TR-PIV with the hot-wire as a reference exhibit a closer match with idealised noise-free DNS cut-offs, with the agreement improving as the distance from the wall increases. The crossover point, where the denoised TR-PIV matches the idealised case, marks the wall height beyond which the TR-PIV can be considered effectively "noise-free".

6 Concluding remarks

This study reported the application of TR-PIV to measure the mean velocity, fluctuating components and spectral response in a TBL over an axisymmetric body of revolution. The TR-PIV method was successfully validated against highly resolved hot-wire measurements of the same flow field and DNS of a TBL over a flat plate. By taking into account the spatial filtering of each method and comparing the equivalent DNS spatially filtered data, a direct comparison of the expected turbulence levels was made. For the boundary layer flow over an axisymmetric body of revolution, the mean velocity profiles of all methods were shown to compare well. It was confirmed that inadequate spatial resolution attenuates the measured turbulence levels and was consistent across two locations along the geometry, where the TBL exhibits a ZPG and mild FPG. The attenuation level increased with lower spatial resolution and distance closer to the wall. The small hot-wire ($l^+ = 29$) revealed better-resolved turbulence levels close to canonical flat plate DNS. In the outer-layer portion of the boundary layer ($z^+ \approx 600$ or $z \approx 0.5\delta$), the difference between the DNS and the measured streamwise Reynolds stresses from the hot-wire and TR-PIV was similar ($\approx 3\%$) and of the same order as the measurement uncertainty. Using the DNS as a reference, an effective laser sheet thickness for the TR-PIV was determined and found to be 40% of the measured burn paper thickness and approximately twice the FWHM value predicted by thin lens theory.

The spectral response of the TR-PIV was then analysed, again using the DNS spatially filtered to match the TR-PIV as a reference. The premultiplied spectra provided insight into the wavelength scales contributing to energy content. It was found that the spectral content that could be resolved by the different methods increased monotonically with better spatial resolution. Close agreement between all methods is observed in detecting the large-scale motions with a streamwise wavelength of $\lambda_x^+ > 3000$ throughout the TBL, whereas a better broadband agreement was found in the outer region of the boundary layer ($z^+ \gtrsim 600$), where energetic contributions from small-scale fluctuations are less.

The spectral analysis was able to identify small-scale noise in the TR-PIV. The investigation then turned to appropriate denoising filters to reduce the TR-PIV noise. The implemented denoising filter of Wieneke (2017) reduced small-scale noise. From the comparisons of spectra from the raw and denoised TR-PIV with reference spectra (DNS or hot-wire), a transfer function was derived and used with -1 dB and -3 dB thresholds to establish cut-off wavelengths as a function of wall-normal distance. The premultiplied spectrograms, combined with these cut-off wavelengths, quantified the resolvable flow scales at various wall heights within the TBL. It was found that the TR-PIV spatial resolution significantly limited the cut-off wavelengths (and frequencies). In contrast, the theoretical Nyquist, particle response and interrogation window cut-off wavelengths for the TR-PIV were much lower and generally fell outside the primary energy range. The interrogation window cut-off wavelengths (and corresponding frequencies) significantly underestimated the actual cut-offs because they did not account for the full 3D spatial filtering inherent in TR-PIV.

In the context of "time-resolved" measurement techniques, this study highlights the key factors that influence the capability of wall-bounded TR-PIV measurements. The interplay between spatial resolution (determined by *IW* size and laser sheet thickness) and its effect on small-scale attenuation is crucial, along with inherent TR-PIV noise, temporal resolution, particle response and particle displacements, all varying with wall height. As demonstrated in this study, these factors must be carefully assessed to accurately evaluate the "time-resolved" validity of TR-PIV measurements.

Our results indicate several factors for understanding the limitations of TR-PIV and optimising accuracy in TBL measurements. Future practitioners are encouraged to apply these considerations as actionable guidelines to determine the minimum resolvable scales and improve measurement accuracy across varying boundary layer conditions:

– *Optimise resolution to capture relevant flow scales:* Use high spatial and temporal resolution to capture turbulence

accurately, particularly near the wall where small scales are more pronounced. Low resolution attenuates turbulence signals, particularly close to the wall. For TBLs with strong small-scale energy, set acquisition rates with $t_c^+ < 3$ and particle displacement around $0.14IW_1$ in the freestream (see Appendix B). These requirements may be relaxed for larger-scale or outer TBL flow studies.

- *Validate TR-PIV data:* Cross-check TR-PIV measurements against high-resolution methods (e.g. hot-wire or DNS) where possible. Spatially filter reference data to match TR-PIV conditions to understand the impact of turbulence attenuation and small-scale noise. In the absence of reference data, use the smallest possible *IW* (within limits of seeding density) and higher acquisition rates to mitigate small-scale turbulence attenuation.
- *Determine spatial cut-off wavelengths:* Establish resolvable flow scales from cut-off wavelengths and frequencies, using a -1 dB threshold, by calculating the transfer function with DNS or high-resolution data as references. Report these values as a function of wall height to facilitate cross-study comparisons.
- *Consider 3D spatial filtering effects:* Recognise that cut-off wavelengths based only on the *IW* size can underestimate actual cut-offs, since they do not account for the full 3D spatial filtering inherent in TR-PIV measurements.
- *Apply denoising filters:* Use denoising filters, such as the method of Wieneke (2017), to reduce small-scale noise in TR-PIV data. Verify the denoising by comparing spectra from raw and filtered data against reference data to ensure minimal signal distortion.
- *Account for pressure gradient and Reynolds number variations:* Recognise that variations in pressure gradients (e.g. ZPG vs. FPG) and Reynolds numbers significantly affect small-scale turbulence characteristics, potentially impacting measurement accuracy. Increased Reynolds numbers amplify small-scale turbulence, generally requiring finer spatial and temporal resolutions to capture the added turbulence energy.

These guidelines depend on the application and objectives of the TR-PIV measurement. Criteria may be relaxed for low Reynolds number flows or outer-layer measurements.

Appendix A Reynolds number and pressure gradient effects

The unique experimental dataset and the evolving DNS data enable us to directly compare the effect of the Reynolds number and pressure gradient. In the case of the canonical DNS, we consider the Reynolds number effect alone. Whereas for the asymmetric TBL we consider the same Reynolds number change, while the flow also undergoes a transition from ZPG to FPG, and we assume that the curvature effects are negligible since the curvature parameter remains small ($\delta/a = 0.10$ and 0.14). Matching Re_θ is preferred over Re_τ for comparing boundary layer evolution under varying pressure gradients, as it reflects overall development and is less sensitive to local pressure gradients (Österlund 2000). In contrast, Re_τ is more influenced by near-wall effects and immediate pressure gradients.

We have already shown that at $x/L = 0.45$, the hot-wire captures the majority of spectral energy with minimal attenuation (see Figs. 4 and 6). In the absence of DNS data with matching FPG conditions, we assume that the small hot-wire ($l^+ = 30$) resolves most scales at the downstream FPG location ($x/L = 0.65$). In Fig. 12a, we plot the DNS spectra for both Reynolds numbers and at three wall heights ($z^+ \approx 200$,

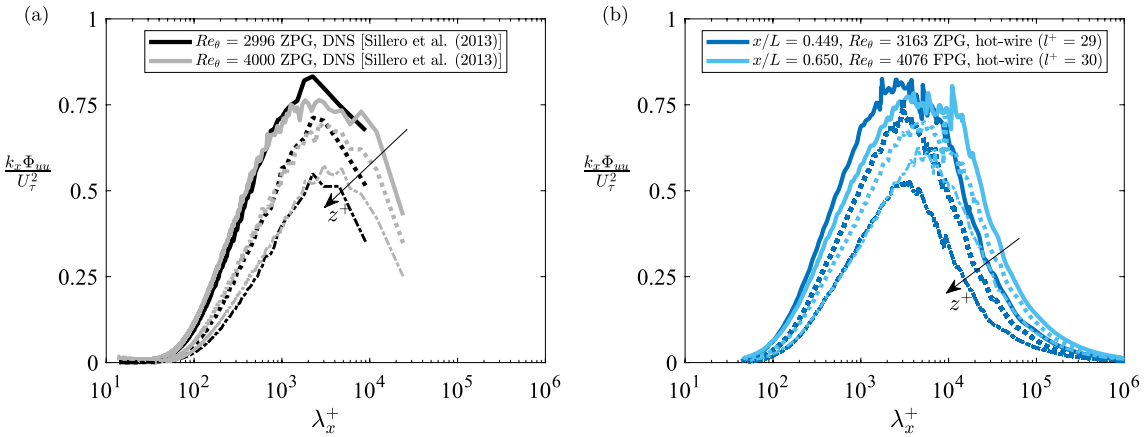

Fig. 12 Effect of Reynolds number on the non-dimensional premultiplied energy spectrogram of streamwise velocity fluctuations, comparing DNS results of a ZPG flat plate TBL from Sillero et al. (2013) (a) with hot-wire measurements from the current study (b), which examines a similar Reynolds number change and the transition from ZPG ($x/L = 0.45$) to FPG ($x/L = 0.65$). Spectra profiles are shown for three wall heights: $z^+ \approx 200$ (solid lines), 400 (dotted lines), and 600 (dash-dot lines)

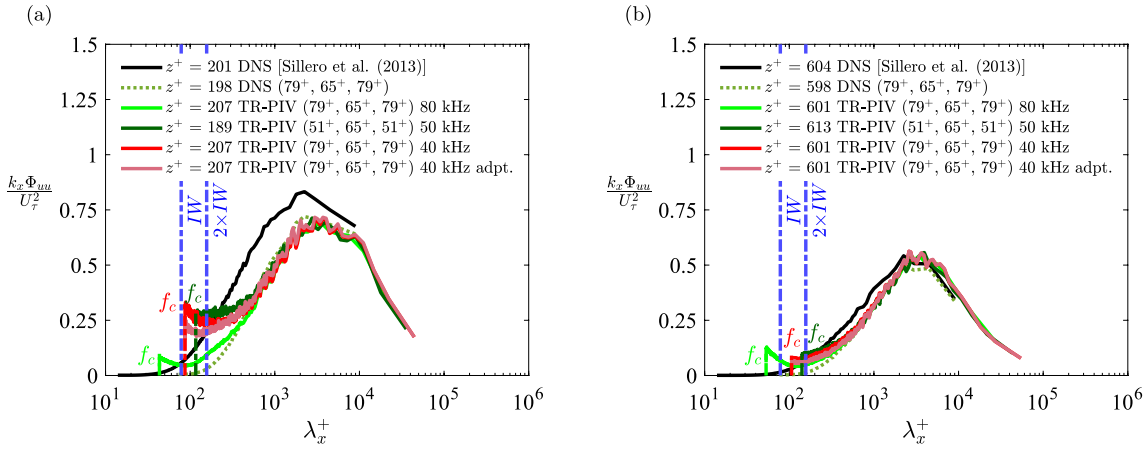

Fig. 13 Comparison of the effect of acquisition frequencies (40 kHz, 50 kHz and 80 kHz) on the energy spectra ($k_x\phi_{uu}/U_\tau^2$) at $x/L = 0.45$ for the ZPG case. The 40 kHz case was also processed using an adaptive *IW* method, labelled as "40 kHz adpt.". For two wall heights: $z^+ \approx 200$ (**a**) and 600 (**b**), the spectra are benchmarked against DNS from Sillero et al. (2013) and spatially filtered DNS matching TR-PIV resolution. The spatial resolution is indicated in the parentheses as (x^+, y^+, z^+). The acquisition cut-off wavelengths (f_c) and interrogation window size cut-off wavelengths (*IW* and $2 \times IW$, dash-dotted blue lines) are also indicated

400 and 600). As Reynolds number increases for the ZPG TBL, small scales remain consistent, as seen in the overlapping profiles, while large-scale energy rises. In Fig. 12b, we plot the hot-wire spectra for the $x/L = 0.45$ and 0.65 at the same wall heights. For the same Reynolds number increase while the flow transitions from a ZPG to an FPG, we observe a reduction in small-scale magnitudes at $z^+ \approx 200$ and 400, which is accompanied by a shift towards larger scales across the three wall heights. At $z^+ \approx 600$, in Fig. 12b, small-scale energy overlaps across axial locations, aligning with the ZPG DNS spectra shown in Fig. 12a. Despite the increase in Re_θ, there is less small-scale energy closer to the wall in the FPG compared with the ZPG case. This result has implications for the acquisition frequencies and temporal resolution effects, which will be explored in the following section.

For the raw TR-PIV results, a larger spread in the $|\ TF\ |$ profiles was found between the near-wall and outer-layer measurements for the ZPG case compared with the FPG case (see Fig. 9 a, b). This may be attributed to the more prominent noise (i.e. "kick-up") in the TR-PIV results for the ZPG case, and given the result above, is likely due to the influence of small scales on the measurement accuracy, as the small scales contribute more to the energy content in the ZPG case compared with the FPG case.

Appendix B TR-PIV: temporal resolution and particle displacement effects

The effects of temporal resolution on the TR-PIV were assessed for the ZPG case at $x/L = 0.45$ by examining spectral responses at acquisition rates of 40, 50, and 80 kHz. Due to the single-cavity laser used, changes in acquisition frequency impact both temporal resolution and particle displacement between images, complicating the ability to isolate these effects. Nonetheless, the analysis offers valuable insights into temporal resolution and particle displacement effects on TR-PIV results.

For reliable particle detection between cross-correlated windows, particle displacement should ideally remain below one-quarter of the initial interrogation window (IW_1) size (Keane and Adrian 1991; Scharnowski and Kähler 2020). For our IW_1 of 64 px × 64 px, this sets a streamwise displacement limit of 16 px at the freestream region. Therefore, it is useful to express imaged particle displacements as a fraction of IW_1. In subsequent passes, the *IW* size is reduced to a final size of 24 px × 24 px, while using the particle image shift from the first pass and image deformation to account for the local displacement gradient. In boundary layer flow with high in-plane velocity gradients near the wall, a larger IW_1 can introduce bias by capturing the faster mean flow farther from the wall, potentially missing smaller fluctuations closer to the wall. This may lead to loss of correlation or the underestimation of small-scale fluctuations, artificially raising noise levels. Employing an adaptive or deformation *IW* scheme may mitigate these effects (Scharnowski and Kähler 2020), as attempted here.

For acquisition rates of 40, 50, and 80 kHz (t_c^+ values of 4.8, 3.9, and 2.4), freestream particle displacements were 18.2 px ($0.28IW_1$), 23.0 px ($0.36IW_1$), and 9.10 px ($0.14IW_1$), respectively. Notably, the spatial resolution was increased to 38.88 px/mm for the 50 kHz case (compared to 24.62 px/mm for the 40 and 80 kHz cases), leading to a higher displacement for 50 kHz than 40 kHz. In Fig. 13, we compare the premultiplied energy spectra of streamwise velocity fluctuations for the ZPG case at two wall-normal

heights of $z^+ \approx 200$ and $z^+ \approx 600$. The 40 and 50 kHz cases at $z^+ \approx 200$ show increased small-scale noise, as seen by the larger "kick-up" in the spectra at $\lambda_x^+ \lesssim 1000$ compared to the 80 kHz case, which adheres to recommended temporal criteria of $t_c^+ < 3$. However, at $z^+ \approx 600$, small-scale noise levels are similar across all acquisition rates. This increased noise in the lower wall-normal region is likely due to larger particle displacements in the 40 and 50 kHz cases. As discussed earlier, large particle displacements can introduce bias errors due to local flow gradients and accelerations. This may reduce correlation when particles exit the *IW* or move out of the light sheet plane (Scharnowski and Kähler 2020). A similar effect was also observed when using suboptimal *IW* sizes (e.g. 16 px × 16 px, not shown) for the 80 kHz case, where insufficient particle counts led to a loss of correlation, amplifying small-scale noise levels and resulting in a more pronounced spectral "kick-up". In the 50 kHz case, with higher spatial resolution ($51^+, 65^+, 51^+$ in x^+, y^+, z^+), the spectral profiles in Fig. 13a, b closely aligns with those of the 40 kHz case, which has lower resolution ($79^+, 65^+, 79^+$). The freestream particle displacements for these cases were 23.0 px ($0.36IW_1$) and 18.2 px ($0.28IW_1$), respectively, suggesting that increased particle displacement can offset the gains from higher spatial resolution. Additionally, maintaining a final *IW* of 24 px but starting with a larger initial IW_1 of 96 px (not shown), which corresponds to a freestream displacement of $0.24IW_1$ for the 50 kHz case, resulted in no obvious reduction in noise. For the 40 kHz case, the adaptive *IW* method of Wieneke and Pfeiffer (2010) was applied, which adjusts the aspect ratio (up to a maximum of 4:1 or 1:4) and the orientation of elliptical window weightings based on local flow gradients. This case is labelled "40 kHz adpt." in Fig. 13. While the adaptive method effectively reduced small-scale noise levels, confirming its association with high-velocity gradients across the *IW*, the noise levels remained higher than those observed in the 80 kHz case.

In Fig. 13, we also show the acquisition cut-off wavelengths (f_c) for each case and the interrogation window cut-offs (*IW* and $2 \times IW$, vertical dash-dotted blue lines). Beresh (2021) highlights that aliasing noise effects are more prevalent in cases where the spatial frequency ($1/IW$) is significantly higher than the temporal frequency (f_c). In our 40 and 50 kHz cases, the *IW* cut-off is slightly smaller (representing higher spatial frequency) than the f_c wavelength cut-off. This moderate discrepancy appears to contribute to increased noise (or aliasing), consistent with the general observation of Beresh (2021).

Our study indicates that flows with significant small-scale energy content, such as ZPG boundary layers, are especially sensitive to temporal resolution and particle displacement. For these cases, adhering to recommended temporal criteria, such as $t_c^+ < 3$ and maintaining particle displacements well below the $0.25IW_1$ threshold—around $0.14IW_1$ in our study—is crucial to mitigate noise and minimise temporal resolution effects on the velocity measurements.

Appendix C Uncertainty quantification

The uncertainty quantification accounts for the primary sources of uncertainty specific to each test technique. As previously mentioned, according to the guidelines in Barlow et al. (1999), the total blockage of the test model resulted in less than a 1% change in flow speed, which was subsequently used to correct the incoming freestream velocity. Additionally, the uncertainty in determining the wind tunnel speed, based on reference instrumentation—comprising the differential pressure across the contraction and tunnel temperature—was ± 0.16 m/s at a speed of 30 m/s (Manovski et al. 2014).

C.1 Uncertainty in TR-PIV measurements

For the TR-PIV method, the bias, and random uncertainty components are determined based on the methodology in Manovski et al. (2014), Manovski et al. (2021). The bias uncertainty, ϵ_b/U_∞ is estimated by the combination of the length scale calibration (δ_l), the laser and camera timing (δ_t) and the in-plane displacement (δ_{xz}), viz.,

$$\frac{\epsilon_b}{U_\infty} \simeq \sqrt{\left(\frac{\delta_t}{\Delta t}\right)^2 + \left(\frac{\delta_l}{(R_l/M)}\right)^2 + \left(\frac{\delta_{xz}}{\Delta x}\right)^2}, \tag{6}$$

where the terms on the right side of are described below:

- For the uncertainty in the laser and camera timing, we account for both the laser's electronic jitter (1 ns) and the minimum clock resolution of the programmable timing unit (1 ns). Combining these uncertainties in quadrature for two pulses yields a total timing uncertainty of $\delta_t = 4$ ns. As a reference time interval, we use the time between laser pulses, Δt, which ranges from 12.5 µs to 25 µs for acquisition rates of 80 kHz and 40 kHz, respectively. Consequently, the relative timing uncertainty is $\delta_t/\Delta t \simeq \pm 0.003$.
- For the uncertainty in the calibration or length scale, we used two graduations on a ruler with a reference length of $R_l = 60$ mm. The accuracy of selecting each graduation was estimated to be ±1 px. The out-of-plane alignment was achieved using a spirit level with an accuracy of 0.005 (in/in) over a 150 mm distance, resulting in a relative out-of-plane uncertainty of ±1.9 px. By combining the in-plane and out-of-plane uncertainties in quadrature and normalising by the reference

length, we arrive at a relative calibration uncertainty, $\delta_l/(R_l/M) \simeq 4\,\text{px}/(60\,\text{mm}/(24.62\,\text{mm/px}) \simeq \pm 0.002$, where M is the image magnification.

– For the uncertainty in the in-plane ($x-z$) displacement, we use the DaVis software, which uses the methods of Wieneke (2015) and Sciacchitano and Wieneke (2016), to calculate the uncertainty of individual displacement values. As an upper bound, the instantaneous uncertainty using this approach revealed maximum values averaging 0.2 px within the log layer, whereas in the outer layer and the freestream region the uncertainty was below 0.1 px. For the reference displacement, we take the smallest freestream displacement, which corresponds to the 80 kHz case, $\Delta x \simeq 8.9\,\text{px}$. Consequently, the maximum total displacement uncertainty is $\delta_{xz}/\Delta x \simeq 0.2/8.9 \simeq 0.022 \simeq \pm 0.011$.

By substituting the individual uncertainties in Eq. 6, gives the bias uncertainty $\epsilon_\text{b}/U_\infty \simeq \pm 0.011$. This corresponds to an estimated instantaneous velocity uncertainty for the TR-PIV of ±1.1% or ± 0.32 m/s. This corresponds to an estimated instantaneous velocity uncertainty for the TR-PIV of ±2.3% or ± 0.65 m/s. The estimated TR-PIV bias uncertainty fails to account for any bias errors or attenuation in turbulence levels due to the spatial resolution, which are analysed in Sect.5.2.

In TR-PIV, velocity measurements are correlated, making it incorrect to use the total sample size (N) to estimate random uncertainties. Instead, the effective sample size (N_eff) is used, as determined by the number of samples separated by the integral timescale (Γ_{uu}), following the approach suggested by Sciacchitano and Wieneke (2016). Subsequently, Smith et al. (2018) demonstrated that N_eff is a suitable method for assessing the uncertainty of dependent samples, provided that the autocorrelation, used to calculate Γ_{uu}, is accurately calculated over sufficiently long records (greater than $20\Gamma_{uu}$). In our case, the data records extend well beyond $10^4\Gamma_{uu}$. Using the TR-PIV time series, integral timescales were calculated at various wall heights for both axial locations by integrating the time-delay correlation coefficient above a threshold value of 3%. At $x/L = 0.45$, the maximum integral timescale was observed at a wall height of $z^+ \approx 200$, with $\Gamma_{uu} = 4.5 \times 10^{-4}\,\text{s}$, yielding an effective sample size of $N_\text{eff} \approx 11,200$ from a total of 800,000 samples. At $x/L = 0.65$, the maximum timescale was found at $z^+ \approx 400$, with $\Gamma_{uu} = 6.4 \times 10^{-4}\,\text{s}$, resulting in $N_\text{eff} \approx 7,800$ from a total of 800,000 samples.

Assuming statistically independent samples (using N_eff) that follow a normal distribution, and based on the theory of random variables for a 95% confidence interval, where the coverage factor $s_c = 2$, the total normalised uncertainty in the ensemble-averaged mean velocity is a combination of both the bias uncertainty (ϵ_b) and the random uncertainty (ϵ_r):

$$\frac{\epsilon_U}{U_\tau} \simeq s_c \sqrt{\frac{1}{N_\text{eff}}\left[\left(\frac{\epsilon_\text{b}}{U_\tau}\right)^2 + \left(\frac{\epsilon_\text{r}}{U_\tau}\right)^2\right]}. \tag{7}$$

Here, ϵ_r represents the random (precision) uncertainty caused by flow unsteadiness, taken as the maximum standard deviation of the ensemble average ($\epsilon_\text{r} \approx 2.5$ m/s), observed at the measurement point closest to the wall. We only consider the bias sources of error that contribute to the statistical uncertainty (outlined in Eq. 6), while disregarding other systematic bias sources that are independent and more challenging to quantify. Substituting the relevant values yields a maximum mean velocity uncertainty for the TR-PIV of ±0.20% or ± 0.06 m/s.

The total normalised uncertainty for the ensemble-averaged streamwise Reynolds stress is estimated using the uncertainty of variances as described by Bendat and Piersol (2010),

$$\frac{\epsilon_{uu}}{U_\tau^2} \simeq \sqrt{\frac{2}{(N_\text{eff}-1)}\left[\left(\frac{\epsilon_\text{b}}{U_\tau}\right)^2 + \left(\frac{\epsilon_\text{r}}{U_\tau}\right)^2\right]}. \tag{8}$$

Substituting the values results in a maximum normalised streamwise Reynolds stress uncertainty $\epsilon_{uu^+\text{max}} = \pm 0.039$ (±3.9%). The uncertainty drops significantly in the outer layer, for example at $z^+ \approx 600$, $\epsilon_{uu^+} = \pm 0.028$ (±2.8%).

For the wall-normal components of the mean velocity and Reynolds stress, we assume that the uncertainty is identical to the streamwise component uncertainties.

C.2 Uncertainty in hot-wire measurements

A study on computer-controlled hot-wire anemometry by Jørgensen (1996) concluded that, with careful attention to calibration, signal conditioning and digitisation, computer-based anemometry can achieve accuracy within a ±1% margin of error for single-wire configurations. Similarly, the uncertainty quantification in hot-wire measurements by McCarthy et al. (2020) under comparable experimental conditions to this study yielded a total uncertainty of approximately ±0.8%, corresponding to ±0.008 or ±0.23 m/s. As with TR-PIV, the uncertainty estimate does not account for the effects of attenuation due to spatial resolution. The uncertainty in streamwise Reynolds stress measurements was found to be approximately ±0.025 or ± 2.5%.

C.3 Uncertainty in spectra

In the spectral analysis of this study, the PSD is estimated using the Welch method (Welch 1967). The PSD estimate, $\Phi(f)$, is derived by averaging the periodograms of overlapping signal segments. MATLAB's `pwelch` function was used to calculate both the PSD and the confidence intervals, which are computed based on the Chi-square distribution (Welch 1967). For a given estimated PSD $\Phi(f)$ at frequency f, the confidence interval is calculated as:

$$\frac{k_f \cdot \Phi(f)}{\chi^2_{1-\alpha/2,k_f}} \leq \Phi(f) \leq \frac{k_f \cdot \Phi(f)}{\chi^2_{\alpha/2,k_f}}, \tag{9}$$

where

- $\Phi(f)$ is the estimated PSD at frequency f.
- k_f is the degrees of freedom, typically calculated as $k_f = 2 \times$ number of segments. When windows overlap, the degrees of freedom become slightly less than $2{\times}k_f$, which introduces minor errors in the confidence intervals. These errors are small when using windows such as Hamming with 50% overlap (our case) but can grow with greater overlap. For the case where there is no overlap, the equation holds exactly.
- $\chi^2_{p_r,k_f}$ is the value from the Chi-square distribution for probability p_r and degrees of freedom k_f.
- α is the confidence level, where we use a 95% confidence interval, $\alpha = 0.05$.

Using this method, a maximum uncertainty within the PSD over the range of frequencies, for a wall height of $z^+ \approx 200$, was $\pm$ 5.0% for the TR-PIV and $\pm$ 2.9% for the hot-wire, occurring in the large scales ($\lambda_x^+ \approx 20^3$) near the peak in energy content. On either side of this peak, the uncertainty was significantly lower. The reduced uncertainty in the hot-wire data is attributed to its longer acquisition period (30 s) compared to the 10 s used for TR-PIV, allowing for greater statistical averaging and thus reduced variability in the PSD estimate.

The contribution of velocity measurement uncertainty to the overall PSD uncertainty includes both bias and random errors. The bias component can be split into systematic bias errors, which are difficult to quantify, and bias errors (ϵ_b) of the velocity measurement due to random noise. While the Welch method accounts for random uncertainties due to flow variability, random measurement noise from TR-PIV or hot-wire systems is not explicitly considered. Since the PSD is proportional to the square of the velocity fluctuations, the bias error contribution can be estimated as twice ϵ_b. However, since the Welch method averages multiple spectral estimates from overlapping segments, the influence of random measurement noise on the PSD is reduced by a factor proportional to the inverse square root of the number of effective window segments ($1/\sqrt{N_w}$). For a window segment length of 2^9 for the TR-PIV and 2^{10} for the hot-wire and a 50% overlap, this corresponds to $N_w = 3125$ for the TR-PIV and $N_w = 2343$ for the hot-wire measurements. Therefore, the adjusted bias PSD uncertainties are approximately 0.02% for both the TR-PIV and hot-wire measurements, which are significantly lower than the PSD uncertainties derived from the Welch method. This suggests that the uncertainty introduced by the spectral transformation is the dominant contributor to the overall PSD uncertainty, while the contribution from velocity measurement uncertainty is minimal.

This analysis neglects the systematic bias uncertainty in both velocity measurements, as the PSD was calculated based on velocity fluctuations with zero mean. Systematic bias uncertainty primarily affects the absolute velocity measurement, but since velocity fluctuations inherently remove the mean component (bias), its influence on the PSD is minimised. Furthermore, we assume that the bias uncertainty remains constant over time, implying that any systematic offset in the velocity measurement does not introduce additional variability into the fluctuation spectrum. However, as noted in Sects. 5.3 and 5.4, we observe that there is a bias error (including attenuation and TR-PIV noise) that correlates with the temporal or spectral characteristics of the velocity field, particularly affecting the small scales. Nonetheless, for the purpose of this uncertainty quantification, this effect is considered negligible, as the maximum PSD uncertainty was found in the large scales ($\lambda_x \gtrsim 2000$), where the attenuation and TR-PIV noise were minimal.

Supplementary Information The online version contains supplementary material available at https://doi.org/10.1007/s00348-025-04059-0.

Acknowledgements The authors would like to extend their gratitude to Simon Henbest, Yu Xia, Malcolm Jones, Jesse McCarthy and Dominic Loveday for their assistance in conducting this investigation and Jelle Will and Mogeng Li for assistance with OFI. Thank you to Rahul Deshpande for assistance in extracting the DNS dataset and fruitful discussions. The authors would also like to thank Sillero et al. (2013) for making the DNS dataset available.

Author contributions P.M. contributed to conceptualisation, methodology, all experiments, data curation, software, validation, formal analysis, investigation, generation of all tables and figures, writing—main manuscript text, visualisation, response to reviewers, updated manuscript, review, and editing. W.A.R. contributed to HWA experimentation, data curation, writing—review and editing. H.N. contributed to HWA and OFI experimentation, data curation. P.G. contributed to TR-PIV experiments. M.G. contributed to writing—review and editing, supervision. C.S. contributed to writing—review and editing, supervision. N.H. contributed to writing—review and editing, supervision. I.M. contributed to writing—review and editing, supervision.

Funding Open Access funding enabled and organized by CAUL and its Member Institutions.

Data availability No datasets were generated or analysed during the current study.

Declarations

Conflict of interest The authors declare that there are no conflict of interest, financial or otherwise, and no relevant declarations or conflict of interest related to the content of this article.

References

Atkinson C, Buchmann NA, Amili O, Soria J (2013) On the appropriate filtering of PIV measurements of turbulent shear flows. Exp Fluids 55(1):1654. https://doi.org/10.1007/s00348-013-1654-8

Atkinson C, Buchmann NA, Soria J (2015) An experimental investigation of turbulent convection velocities in a turbulent boundary layer. Flow Turbul Combust 94(1):79–95. https://doi.org/10.1007/s10494-014-9582-0

Barlow J, Rae W, Pope A (1999) Low-speed wind tunnel testing. In: Aerospace engineering, mechanical engineering. Wiley. https://books.google.com.au/books?id=LBMoAQAAMAAJ

Bendat J, Piersol A (2010) Random data: analysis and measurement procedures. Wiley, New York

Beresh SJ (2021) Time-resolved particle image velocimetry. Meas Sci Technol 32(10):102003. https://doi.org/10.1088/1361-6501/ac08c5

Chin CC, Hutchins N, Ooi ASH, Marusic I (2009) Use of direct numerical simulation (DNS) data to investigate spatial resolution issues in measurements of wall-bounded turbulence. Meas Sci Technol 20(11):115401. https://doi.org/10.1088/0957-0233/20/11/115401

de Kat R, Ganapathisubramani B (2015) Frequency-wavenumber mapping in turbulent shear flows. J Fluid Mech 783:166–190. https://doi.org/10.1017/jfm.2015.558

Erm LP (2003) Calibration of the flow in the extended test section of the low-speed wind tunnel at DSTO. Technical Report DSTO-TR-1073, Defence Science and Technology Organisation, Australia

Foucaut JM, Carlier J, Stanislas M (2004) PIV optimization for the study of turbulent flow using spectral analysis. Meas Sci Technol 15(6):1046. https://doi.org/10.1088/0957-0233/15/6/003

Grayson K, de Silva CM, Hutchins N, Marusic I (2017) Impact of mismatched and misaligned laser light sheet profiles on PIV performance. Exp Fluids 59(1):2. https://doi.org/10.1007/s00348-017-2453-4

Hutchins N, Nickels TB, Marusic I, Chong MS (2009) Hot-wire spatial resolution issues in wall-bounded turbulence. J Fluid Mech 635:103–136. https://doi.org/10.1017/S0022112009007721

Hutchins N, Monty J, Hultmark M, Smits A (2015) A direct measure of the frequency response of hot-wire anemometers: temporal resolution issues in wall-bounded turbulence. Exp Fluids 56:01. https://doi.org/10.1007/s00348-014-1856-8

Jørgensen FE (1996) The computer-controlled constant-temperature anemometer. Aspects of set-up, probe calibration, data acquisition and data conversion. Meas Sci Technol 7(10):1378. https://doi.org/10.1088/0957-0233/7/10/008

Joubert PN (2006) Some aspects of submarine design part 2: shape of a submarine. Technical Report DSTO-TR-1622, Defence Science and Technology Organisation, Australia

Kähler C, Sammler B, Kompenhans J (2002) Generation and control of tracer particles for optical flow investigation in air. Exp Fluids 33:736–742. https://doi.org/10.1007/s00348-002-0492-x

Kähler CJ, Scharnowski S, Cierpka C (2012) On the resolution limit of digital particle image velocimetry. Exp Fluids 52(6):1629–1639. https://doi.org/10.1007/s00348-012-1280-x

Keane RD, Adrian RJ (1991) Optimization of particle image velocimeters: Ii. multiple pulsed systems. Meas Sci Technol 2(10):963. https://doi.org/10.1088/0957-0233/2/10/013

Kumar P, Mahesh K (2018) Large-eddy simulation of flow over an axisymmetric body of revolution. J Fluid Mech 853:537–563. https://doi.org/10.1017/jfm.2018.585

Manovski P, Giacobello M, Jacquemin P (2014) Smoke flow visualisation and particle image velocimetry measurements over a generic submarine model. Technical Report DSTO-TR-2944, Defence Scienct and Technology Organisation, Australia

Manovski P, Jones M, Henbest S, Xue Y, Giacobello M, de Silva C (2020) Boundary layer measurements over a body of revolution using long-distance particle image velocimetry. Int J Heat Fluid Flow 83:108591. https://doi.org/10.1016/j.ijheatfluidflow.2020.108591

Manovski P, Novara M, Depuru-Mohan K, Geisler R, Schanz D, Agocs J, Godbersen P, Schröder A (2021) 3D lagrangian particle tracking of a subsonic jet using multi-pulse shake-the-box. Exp Therm Fluid Sci 123:110346. https://doi.org/10.1016/j.expthermflusci.2020.110346

Manovski P, Gulotta P, de Silva C, Brown R, Giacobello M, Hutchins N, Marusic I (2022a) Particle tracer analysis for PIV experiments in a closed loop transonic wind tunnel. In: 20th International symposium on application of laser and imaging techniques to fluid mechanics, Lisbon, Portugal

Manovski P, Ng H, Giacobello M, de Silva C, Abu Rowin W, Hutchins N, Marusic I (2022b) Cross-validation of turbulent boundary layer measurements over an axisymmetric body of revolution. In: 23rd Australasian fluid mechanics conference, Sydney, Australia

Manovski P, Loveday D, Ng H, Giacobello M, de Silva C, Hutchins N, Marusic I (2023) Turbulent boundary layer measurements in the presence of pressure gradients and curvature. In: 15th international symposium on particle image velocimetry, San Diego, USA

McCarthy J, Teske T, Jones M (2020) Additive manufacturing pressure-tapped metallic models for wind tunnel testing at DST Group. Technical Report DST-Group-TR-3718, Defence Scienct and Technology Group, Australia

Mei R (1996) Velocity fidelity of flow tracer particles. Exp Fluids 22(1):1–13. https://doi.org/10.1007/BF01893300

Mullin JA, Dahm WJA (2005) Dual-plane stereo particle image velocimetry (DSPIV) for measuring velocity gradient fields at intermediate and small scales of turbulent flows. Exp Fluids 38(2):185–196. https://doi.org/10.1007/s00348-004-0898-8

Österlund JM (2000) Experimental studies of zero pressure-gradient turbulent boundary layer flow. Sweden, Royal Institute of Technology, Department of Mechanics, Stockholm

Piquet J, Patel V (1999) Transverse curvature effects in turbulent boundary layer. Prog Aerosp Sci 35(7):661–672. https://doi.org/10.1016/S0376-0421(99)00007-X

Raffel M, Kähler C, Willert C, Wereley S, Scarano F, Kompenhans J (2018) Particle image velocimetry: a practical guide. 3rd edn. Springer, Germany https://doi.org/10.1007/978-3-319-68852-7

Ragni D, Schrijer F, van Oudheusden BW, Scarano F (2011) Particle tracer response across shocks measured by PIV. Exp Fluids 50(1):53–64. https://doi.org/10.1007/s00348-010-0892-2

Renard N, Deck S (2015) On the scale-dependent turbulent convection velocity in a spatially developing flat plate turbulent boundary layer at Reynolds number $re_\theta = 13\,000$. J Fluid Mech 775:105–148. https://doi.org/10.1017/jfm.2015.290

Saleh B, Teich M (2019) Fundamentals of photonics, 3rd edn. Wiley.

Samimy M, Lele SK (1991) Motion of particles with inertia in a compressible free shear layer. Phys Fluids A 3(8):1915–1923. https://doi.org/10.1063/1.857921

Scarano F (2001) Iterative image deformation methods in PIV. Meas Sci Technol 13(1):R1. https://doi.org/10.1088/0957-0233/13/1/201

Scharnowski S, Kähler CJ (2020) Particle image velocimetry - classical operating rules from today's perspective. Opt Lasers Eng 135:6. https://doi.org/10.1016/j.optlaseng.2020.106185

Schlatter P, Örlü R (2010) Assessment of direct numerical simulation data of turbulent boundary layers. J Fluid Mech 659:116–126. https://doi.org/10.1017/S0022112010003113

Schneiders JFG, Avallone F, Pröbsting S, Ragni D, Scarano F (2018) Pressure spectra from single-snapshot tomographic PIV. Exp Fluids 59(3):57. https://doi.org/10.1007/s00348-018-2507-2

Schrijer FFJ, Scarano F (2008) Effect of predictor-corrector filtering on the stability and spatial resolution of iterative PIV interrogation. Exp Fluids 45(5):927–941. https://doi.org/10.1007/s00348-008-0511-7

Sciacchitano A, Wieneke B (2016) PIV uncertainty propagation. Meas Sci Technol 27(8):084006. https://doi.org/10.1088/0957-0233/27/8/084006

Sillero JA, Jiménez J, Moser RD (2013) One-point statistics for turbulent wall-bounded flows at Reynolds numbers up to $\delta^+ \approx 2000$. Phys Fluids 25(10):105102. https://doi.org/10.1063/1.4823831

Smith BL, Neal DR, Feero MA, Richards G (2018) Assessing the limitations of effective number of samples for finding the uncertainty of the mean of correlated data. Meas Sci Technol 29(12):125304. https://doi.org/10.1088/1361-6501/aae91d

Squire DT, Morrill-Winter C, Hutchins N, Marusic I, Schultz MP, Klewicki JC (2016) Smooth- and rough-wall boundary layer structure from high spatial range particle image velocimetry. Phys Rev Fluids 1:064402. https://doi.org/10.1103/PhysRevFluids.1.064402

Stanislas M, Okamoto K, Kähler C, Westerweel J (2005) Main results of the second international PIV challenge. Exp Fluids 39:170–191. https://doi.org/10.1007/s00348-005-0951-2

Theunissen R, Stitou A, Riethmuller M (2008) A novel approach to improve the accuracy of PTV methods. In: 12th international symposium on application of laser techniques to fluid mechancis, Lisbon, Portugal, vol 08

Welch P (1967) The use of fast Fourier transform for the estimation of power spectra: a method based on time averaging over short, modified periodograms. IEEE Trans Audio Electroacoust 15(2):70–73. https://doi.org/10.1109/TAU.1967.1161901

Wieneke B (2015) PIV uncertainty quantification from correlation statistics. Meas Sci Technol 26(7):074002. https://doi.org/10.1088/0957-0233/26/7/074002

Wieneke B (2017) PIV anisotropic denoising using uncertainty quantification. Exp Fluids 58(8):94. https://doi.org/10.1007/s00348-017-2376-0

Wieneke B, Pfeiffer K (2010) Adaptive PIV with variable interrogation window size and shape. In: 15^{th} international symposium on applications of laser techniques to fluid mechanics. Libson, Portugal. https://api.semanticscholar.org/CorpusID:174777310

Willert CE (2015) High-speed particle image velocimetry for the efficient measurement of turbulence statistics. Exp Fluids 56(1):17. https://doi.org/10.1007/s00348-014-1892-4

Willert CE (2018) "Profile-PIV" – more than just an optical hotwire: new potentials of particle image velocimetry in boundary layer research. In: 18th international symposium on flow visualization, Zurich, Switzerland, vol 06 https://doi.org/10.3929/ethz-b-000280170

Willert CE, Gharib M (1991) Digital particle image velocimetry. Exp Fluids 10(4):181–193. https://doi.org/10.1007/BF00190388